Spatial Distribution and Temporal Evolution of Near-Inertial Waves in Lake Superior

A THESIS
SUBMITTED TO THE FACULTY OF THE GRADUATE SCHOOL
OF THE UNIVERSITY OF MINNESOTA
BY

Lucas J Gloege

IN PARTIAL FULFILLMENT OF THE REQUIREMENTS
FOR THE DEGREE OF
MASTER OF SCIENCE

Advisor : Jay Austin

June, 2014

© Lucas J Gloege 2014
ALL RIGHTS RESERVED

Acknowledgements

Abstract

Numerical modeling and observational data of temperature and currents were used to study the spatial structure and temporal evolution of near-inertial waves (NIWs). A hierarchy of models were ran using ideal wind stress as well as spatially and temporally varying wind stress derived from NARR wind speeds. Results indicate that a wind stress lasting for half an inertial period is most efficient at putting kinetic energy into the system at the Coriolis frequency. Although ideal forcing puts energy in at the Coriolis frequency, it puts about four orders of magnitude less energy in at other frequencies. High energy away from the Coriolis frequency in observations is likely the result of vagaries in the wind field. A model of Lake Superior was ran for the period of July, 1 2011 to September, 19 2011. Lake Superior was modeled as a closed basin and radiative forcing was neglected in the model in order to solely look at the effects of wind stress on inertial currents. Model output was compared with ADCP observations from three mooring sites in Lake Superior.

Contents

Acknowledgements **i**

Abstract **ii**

List of Tables **v**

List of Figures **vi**

1 Introduction **1**

1.1 Background 1

1.1.1 Internal Waves 1

1.1.2 Near-Inertial Waves 2

1.2 Motivation 5

1.3 Lake Superior 7

1.3.1 Thermal Structure 8

2 Mathematical background **12**

2.1 Navier-Stokes Equations 12

2.2 Pure Inertial Oscillations 14

2.3 Poincaré Waves - Single Layer 17

2.4 Poincaré Waves - Double Layer 19

3 Methods **23**

3.1 Modeling 23

3.1.1 Configuration 23

3.1.2 Vertical Structure 26
3.1.3 Forcing 28
3.1.4 Computation 31
3.2 Lake Superior Mooring Array 31
3.3 ADCP 33
3.4 Wavelet Analysis 34
3.5 Near-Inertial Energy 36
3.5.1 Near-Inertial Potential Energy 36
3.5.2 Integrated Kinetic Energy 37

4 Results **39**
4.1 Modeling 39
4.1.1 Ideal Basin : Closed Boundaries 39
4.1.2 Ideal Basin : Periodic Boundaries 44
4.1.3 Lake Superior : Flat Bottom 47
4.1.4 Lake Superior : Realistic Bathymetry 48
4.2 ADCP Observations 51
4.3 Comparison 53

5 Discussion **58**
5.1 Modeling 58
5.2 Near-Inertial Energy 63
5.2.1 Wind Field 63
5.3 Wave Climate 66
5.4 Future Work 67

6 Conclusions **68**
6.1 Conclusions 68

List of Tables

2.1 Navier-Stokes equation variables 13
3.1 Thermal Stratification Values 27
3.2 Mooring Array 33

List of Figures

1.1 Lake Superior Bathymetry 7
1.2 Freshwater Density 8
1.3 Lake Superior Thermal Structure 10
2.1 single-layer-diagram 17
2.2 two-layer-diagram 20
2.3 Observational Spectrums 22
3.1 Arakawa-C Grid Cell 25
3.2 Modeled Initial Thermal Structure 28
3.3 NARR Stress 29
3.4 Core Mooring Stress 30
3.5 NDBC vs NARR 31
3.6 Lake Superior Mooring Array 33
3.7 ADCP Deployment Record 34
3.8 Complex Morlet Wavelet 36
4.1 Temperature Contour 40
4.2 Current Contour 41
4.3 Wavelet Contour 42
4.4 Ideal Spectrums 43
4.5 Ideal Surface Energy 44
4.6 Periodic Temperature Contour 45
4.7 Periodic Current Contour 46
4.8 Periodic Spectrum 47
4.9 Spatial Energy - Flat Bottom 48
4.10 Energy distribution: Realistic Bathymetry 49

4.11 Spatial Energy : Realistic Bathymetry 50
4.12 Wave Climate : Realistic Bathymetry 50
4.13 Core Mooring ADCP Observations 51
4.14 Core Moorings Wavelet 52
4.15 Observational/ Model Comparison 54
4.16 Observational/ Modeled Wavelet Amplitude - WM 55
4.17 Observational/ Modeled Wavelet Amplitude - CM 56
4.18 Observational/ Modeled Wavelet Amplitude - EM 57
5.1 Inertial Energy vs. Stress Duration 59
5.2 Inertial Box Model 61
5.3 Rotary Spectrum Comparison 62
5.4 Zonal Current Comparison 64
5.5 Meridional Current Comparison 65
5.6 Compare Wind Stress and Surface Current 66

Chapter 1

Introduction

1.1 Background

1.1.1 Internal Waves

The Norweigen explorer Fridtjof Nansen made the first observations of internal waves in 1893 while exploring the arctic. Nansen's ship, the Fram, had a reduced motion when sailing atop fresh water. The phenomenon, which Nansen called 'dead water', was a result of a internal wave at the interface between the low density fresh water and high density saline water. The details of the phenomenon were later explained by Ekman (Ekman 1904).

Internal waves occur at pycnoclines in the fluid, because the density difference leads to a gravitational or hydrostatic pressure restoring force if the fluid is displaced vertically. Therefore, a more descriptive term is an internal gravity wave. Two important pycnoclines in the ocean are the halocline (salinity gradient) and the thermocline (temperature gradient), the latter being more important in lacustrine environments. The frequency of internal waves are typically lower than that of surface gravity waves, because density differences within a fluid are usually very small. The wavelength and period of internal waves span a wide range, centimeters to kilometers and seconds to hours respectively. The amplitude of internal waves can be orders of magnitude larger than surface gravity waves.

There is a whole classification of internal waves depending on the fluid stratification,

wave amplitude, and generation mechanism. Interfacial waves propagate along the interface separating fluids of different densities, large amplitude interfacial waves are termed solitary waves (wave of translation) and lee waves are generated by flow over topography. [1] This thesis will focus on near-inertial waves, which are waves whose dynamics are influenced by the Coriolis effect when the wave frequency is comparable to the Earth's rotational frequency.

Two types of basin scale internal waves are typically observed in large lakes, namely Kelvin waves and Poincaré waves. Kelvin waves are shore hugging internal waves which have the most influence between the coast and a distance of one internal Rossby radius. These waves propagate around the the basin of the lake and produce no flow normal to the shore. The amplitude decays off shore exponentially fast, $exp(\frac{-fx}{c})$, where f is the Coriolis frequency, x is the distance from shore, and c is the internal wave speed (Mortimer 1974). Poincaré waves on the other hand produce motion across the entire basin and have little effect near shore (Antenucci and Imberger 2001), this type of wave will be the focus of this thesis.

1.1.2 Near-Inertial Waves

Near-inertial waves (NIWs) are propagating Poincaré waves, in other words, the frequency is super-inertial but close to the inertial frequency. Large wavelength NIWs are commonplace in the ocean and atmosphere. Qi et al. (1995) used the phase difference between moored sites in the ocean to estimate the wavelength of NIWs to be between 80 km - 180 km. Wavelengths on this scale are not permissible in large lakes, such as Lake Superior, since it is comparable to the basin scale. Although wavelengths of this order are not not form at the surface in Lake Superior, NIWS can propagate along sharp density differences in the lake, such as at the thermocline. The (internal) Rossby radius of deformation, defined as $R = \frac{c}{f_o}$, where c is the (internal) wave speed and f_o is the local Coriolis frequency, quantifies the length scale at which rotation becomes important in a basin. For large lakes the Rossby radius at the surface is much larger than the basin scale, therefore NIWs will be weakly observed at the surface in surface water level records. The internal Rossby radius for Lake Superior is on the order of 10

[1] An example of a lee wave is the Sierra wave, which is the result of wind being pushed up the Sierra Nevada mountain range and condensing forming a lenticular cloud downwind.

km, which implies that NIWs can be observed within the lake where pycnoclines are the undulating surface.

Throughout the 1960s and 1970s extensive observations of NIWs were made throughout the Laurentian Great Lakes using moored platforms to collect data on the thermal and current structure of various lakes. Observations of currents were made using vector averaging current meters, such as a geodyne current meter, which correlates the number of revolutions of a rotor in a sampling period to speed. The direction of the rotor at the end of the sampling period is taken to be the direction of the current. These types of measurements are crude compared with observations from an acoustic doppler current profiler, or ADCP, (Bugnon and Whitehouse 1991). An ADCP sends out a pulse of sound which reflects off passively moving particles in the water. The range of the object can be calculated by $R = \frac{1}{2}tc$, where t is the round trip time of the signal and c is the speed of sound in water (≈ 1500 ms^{-1}). The Doppler shifted frequency yields information about the velocity of the moving particle, $f_d = \frac{2v}{c} f_o$, where f_d is the Doppler shift in the original frequency f_o and v is the velocity of the source. The ADCP's transducers are arranged in a Janus pattern, which allows the current vector to broken down into zonal, meridional, and vertical components.

During the International Field Year for the Great Lakes (IFYGL) a comprehensive interdisciplinary study was done on Lake Ontario (McCulloch 1973). A staggered grid of moorings were placed throughout Lake Ontario (average spacing of 15 km), most stations recorded current at 15 and 30 m depth and temperature at 0,10,15,30, and 50 m. However, a few other stations sampled at various other depths. The July 1972 thermal structure showed spectral energy at the inertial frequency (0.057 cycle hr^{-1}) to be greatest at the thermocline and the spatially averaged current to be greatest above the thermocline (Pickett and Richards 1975). The same observation was also observed in Lake Erie (Boyce and Chiocchio 1987). Observations of winter (December 1972 - March 1973) currents in Lake Ontario at 15 and 75 m showed inertial kinetic energy, calculated using band-passed filtered current velocities, to be greater during period of stratification (Marmorino 1978). A similar study with 21 stations in Lake Huron showed that inertial motion was prominent during the stratified period of June-August 1966 and that this motion was clearly defined during periods of strong stratification (Sloss and Saylor 1976). Marmorino (1978) also showed the band-passed current time series at the

15 and 75 m depth to be about 180 degrees out of phase, which shows the baroclinic nature of inertial currents. Blanton (1974) studied the season variation of currents in 1970 throughout the water column in Lake Ontario and showed that inertial currents in the spring (May 16 - June 2), summer (July 4 - July 18), and fall (October 1 - October 19) accounted for about 20%, 50%, and 10% of the variance respectively at a site 16 km offshore. Blanton (1974) also showed that inertial energy decreases closer to shore.

Recent observations in Lake Michigan and Lake Superior have corroborated the findings of these earlier studies. Choi et al. (2012) showed that NIWs were prominent during the stratified season and accounted for about 80% of the surface observations at an open water site in Lake Michigan. Observations in Lake Superior from 2008-2011 show that near-inertial response is related to the strength of stratification and that motion above and below the thermocline are roughly 180 degrees out of phase (Austin 2013). Austin (2013) analyzed NIWs as propagating plane waves and made estimates of the wave climate in Lake Superior. He found the wavelength to vary between 30-60 km and the group speed (speed energy is transferred) to be around 22 cm s^{-1}. An interesting finding made by Austin (2013) was that the direction of these waves slowly veers counterclockwise with a period of about 1 month, which he noted has the same direction and period as the lowest order internal Kelvin wave.

The spatial structure of NIWs is not well characterized and all previous studies have approached the problem with modal analysis. Early work in this area was done by Schwab (1977) in a flat bottom Lake Ontario model. He used a numerical procedure to calculate the amplitude and phase distribution of three Poincaré type modes. Schwab (1977) calculated the three lowest Poincaré modes to have period of 16.8, 16.7, and 16.6 hours. A peak centered at these periods was observed by Pickett and Richards (1975) in the average power spectra of temperature. However, Pickett and Richards (1975) observed spectra of current components to be closer to the inertial period (17.35 hours). Schwab (1977) suggested it would be hard to separate these modes by standard methods and that the observed temperature spectra most likely contained energy from a few modes. Numerical modeling in Lake Michigan by Ahmed et al. (2013) show the spatial structure of dominant internal modes. Analysis of isothermal displacements revealed three nodes in Lake Michigan with clockwise phase propagation around each node. bottom (Gómez-Giraldo et al. 2006).

The partition of energy in NIWs has been of particular interest in Lake Kinneret (Sea of Galilee) (Antenucci and Imberger 2001). Potential energy is carried in undulations of pycnoclines, while kinetic energy is carried in the currents. Large currents are observed in the top mixed layer while weaker currents are observed below the thermocline. This is because the wind stress directly acts on the mixed layer producing larger currents. When the surface water subsides, such as at a coast, the thermocline will be depressed generating a weak return flow in the bottom layer. The resulting oscillations at the thermocline are analogous to surface gravity waves. The ratio of potential to kinetic energy in inertial waves is dependent on the Burger number defined as $Bu = (\frac{R_d}{L})^2$, where R_d is the Rossby radius of deformation and L is the length scale of the basin (Antenucci and Imberger 2001). Antenucci and Imberger note that high Burger number basins have equal partition between potential and kinetic energy while low Burger number basins, such as Lake Superior, have an energy partition dominated by kinetic energy.

1.2 Motivation

The motivation for this thesis stems from the proposed connection between near-inertial waves and the resuspension of nutrients during the stratified season. Near-inertial currents have been correlated with the thickness of the benthic nepheloid layer, suggesting these waves are important drivers resuspending nutrients and sediment (Hawley 2004). Also, autonomous glider observations in Lake Superior show a link between stratification and backscatter of CDOM. (Austin 2013). Therefore, understanding the spatial distribution of near-inertial energy could have ecological significance. In addition, these waves need to be accurately modeled to correctly simulate the dynamics of nutrients, since plankton is observed to move with current and though the action of wave breaking nutrients can be moved into or out of the surface mixed layer.

Very little is known about the spatial structure of near-inertial waves. Studies that have been done analyzed the waves as basin scale normal modes (Schwab 1977, Rueda et al. 2003, Gómez-Giraldo et al. 2006, Ahmed et al. 2013). Schwab (1977) numerically calculated some of the inertial modes for Lake Ontario while Gomez-Giraldo et al. (2006) and Ahmed et al. (2013) used numerical simulations to study the spatial structure of

these waves. Modeling studies have shown that the spatial structure of these waves is too complex to be predicted by internal wave modes and that bathymetry plays an important role in the spatial distribution of energy (Rueda et al. 2003). Because of the complex nature of modal analysis for irregular basins the approach taken in this thesis will follow Austin (2013) and analyze NIWs in terms of the wave climate.

The deep chlorophyll maximum, which tends to coincide with the thermocline, is commonplace in the ocean (Cullen 1982) and during the stratified season in Lake Superior (Barbiero and Tuchman 2004). Internal waves are characterized by undulations of the thermocline and therefore can potentially move phytoplankton rich water downward or, though wave breaking, bring nutrient rich water into the surface mixed layer (Haury et al. 1979) (Haury et al. 1983).

The other motivating factor for this study is to better understand the relationship between wind field and near-inertial wave energy. Using one dimensional models Pollard (1970), Pollard and Millard Jr. (1970) were able to show a few important relationships. The first relationship is that a wind stress acting for less than one inertial period most effectively puts energy into inertial motions (Pollard 1970). Imagine a wind stress acting for one inertial period, the amount of momentum put into the inertial motion during the first half will be taken out during the second half. Therefore, a wind stress acting for half an inertial period effectively puts the most energy into inertial motion. Secondly, a wind stress rotating clockwise in the northern hemisphere (counter-clockwise in the southern hemisphere) will continuously put energy into inertial motions (Pollard and Millard Jr. 1970). For example, if the wind stress were rotating at the inertial frequency then the direction of the wind stress and direction of the current would always be in the same direction and therefore momentum could always be put into the motion. This has been shown in observations as well, Boyce et al.(1987) presented observational evidence that large near-inertial events are associated more with clockwise rotating wind vectors than the amplitude of the wind stress (Boyce and Chiocchio 1987).Todays models do not have the predictive power to determine when and where large inertial events will occur and it is hoped that someday these models can make accurate predictions of when and where large near-inertial events will occur.

1.3 Lake Superior

Lake Superior formed approximately 11,000 years ago as the Laurentide ice sheet retreated northeastward across what is now Canada (Thomas and Dell 1978). Lake Superior is part of the Laurentian Great Lakes System, which also includes Lake Huron; Lake Ontario; Lake Michigan; and Lake Erie. It is the largest lake of the Laurentian Great Lakes by surface area (82,100 km^2) and volume (12,100 km^3).

Worldwide, Lake Superior is the largest lake by surface area and third largest by volume. The lake is also an important water source and holds approximately 20% of the world's freshwater supply. Lake Superior has a length of 560km, and breadth of 260km. The retention time of the lake is about 200 years. The lake is home to 38 native species of fish, including ciscoes, whitefish, and trout.

Lake Superior can be divided into two deep basins separated by a relatively shallow ridge off the Keweenaw peninsula. The average depth of the lake is about 150 m and has a maximum depth of 406 m.

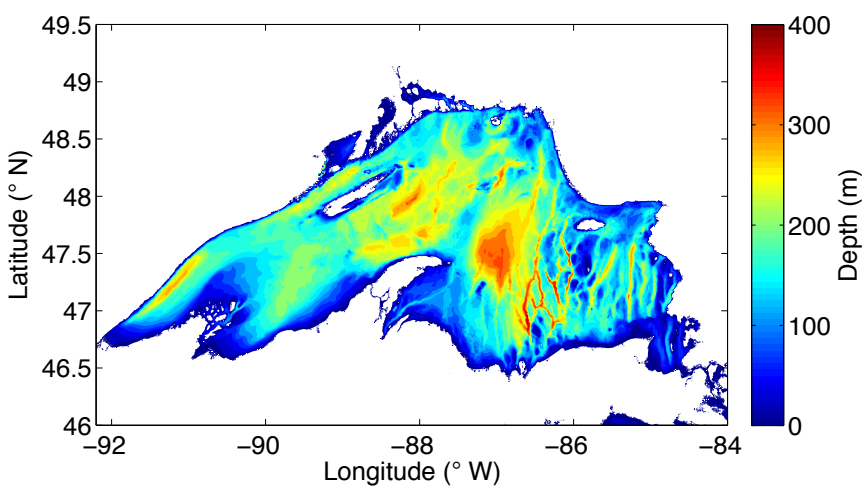

Figure 1.1: **Lake Superior Bathymetry.** Bathymetry of Lake Superior. Mean depth of 150 m and max depth of 406 m. A shallow ridge extending off the Keweenaw Peninsula separates the lake into two deep basins . (source : NOAA)

1.3.1 Thermal Structure

Freshwater lakes stratify because the temperature of maximum density (T_{md}=3.98°C) is greater than the freezing point (T_f=0°C) at zero gauge pressure. T_{md} decreases as pressure increases therefore, T_{md} is lower at greater depth. A plot of freshwater density vs temperature is given below.

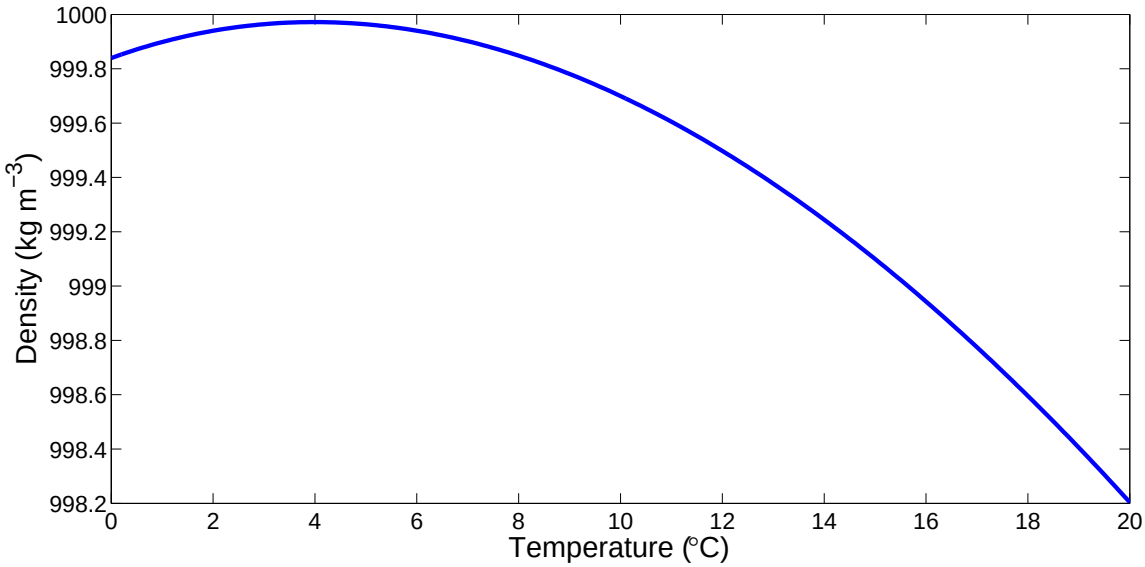

Figure 1.2: **Freshwater Density.** Fresh water density as a function of temperature at zero gauge pressure (Chen and Millero 1986).

Lets assume the entire water column is T_{md}, surface heat fluxes will then cause the surface of the lake to warm or cool away from T_{md} and this less dense water will float atop the more dense water below. Water nearest to the bottom of the lake will remain very close to T_{md} throughout the entire year. As more and more heat enters the surface of the lake the water column will separate into two distinct layers. The epilimnion, or surface mixed layer, and the more stagnant hyplimnion below. At the intersection between these two layers is the metalimnion, which is characterized by the thermocline or sharp temperature/density gradient. As the epilimnion heats up the

density difference between the two layers increases leading to a steeper and more stable thermocline.

Just after stratification the hypolimnion is rich in oxygen from the spring mixing. Since the epilimnion acts as a barrier to the hypolimnion, deep water is cut off from oxygen exchange with the atmosphere and therefore this region can become anoxic as oxygen is consumed by bottom dwellers. During stratification the lake can partially mix as cold fronts pass over with high winds.

The beginning of stratification varies around the lake, typically late June near the shore and mid-July in open water. November is typically the end of the stratified season. With global temperature increasing it is likely to expect stratification to start early and have a prolonged period of stratification. Negative stratification occurs in the winter. The bottom of the lake remains close the temperature of maximum density while surface water is colder and less dense, hence this water floats atop the dense deep water. However, water freezes at $0°C$ so the density difference between these two layers is very small, but is enough to change the dynamics of the water column. During the summer stratified season the density difference between the surface and bottom is close to $20 * 10^{-4}$g cm^{-3} and during the winter when the lake is inversely stratified this density difference is around $5 * 10^{-4}$g cm^{-3}. Lake Superior is a dimicitic lake and therefore stratifies twice pear year, once in summer and once in winter. The thermal cycle in Lake Superior is provided below at the core mooring sites.

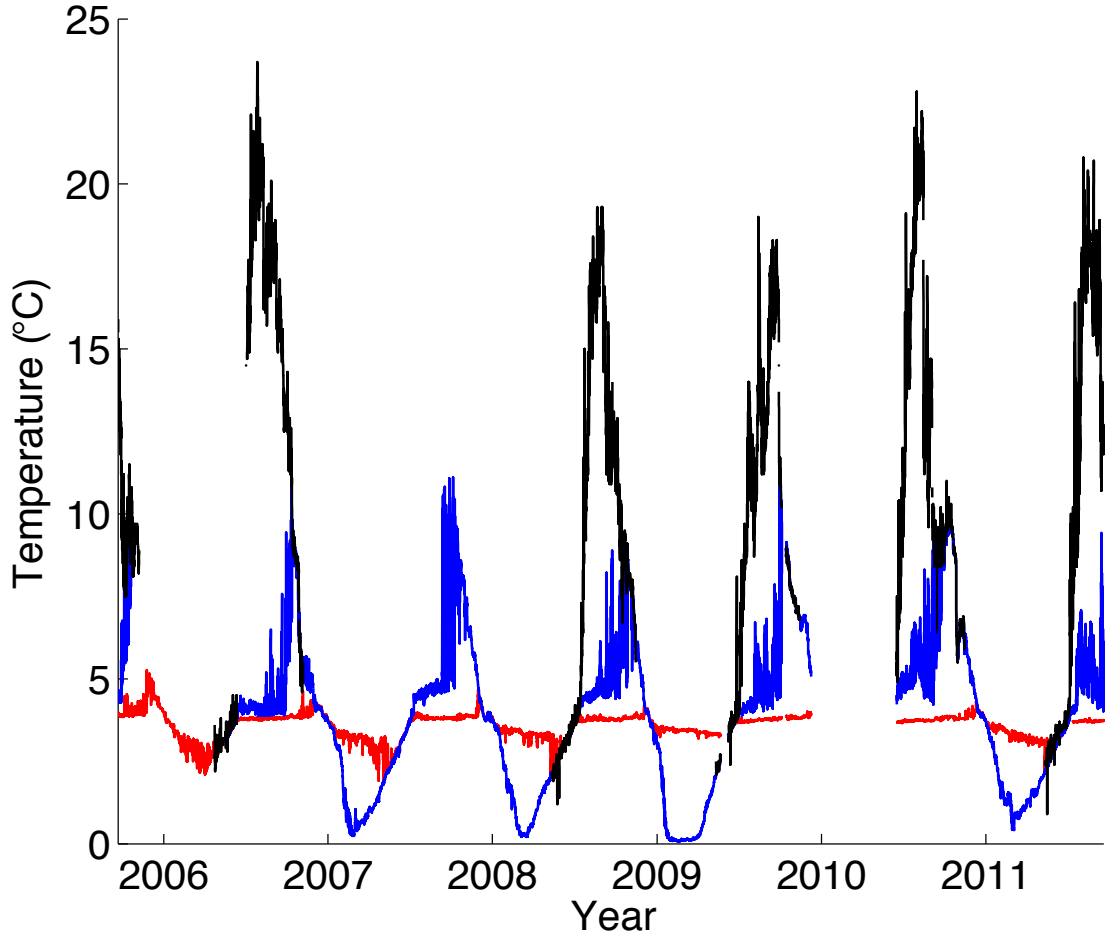

Figure 1.3: **Lake Superior Thermal Structure.** Thermal cycle of Lake Superior. The solid black line shows the epilimnion temperature (measurement taken either 1 or 10 m from the surface) and the dotted red line is the thermistor 250 m from the surface.

The heat content of Lake Superior can be broken down into the "spring heat income" and the "annual heat income", where are described by (Bennett 1978). The spring heat income is the heat gained by the water column moving from a state of minimum winter heat content to the time the water column begins to stratify in the summer. The annual

heat income is the difference between the minimum the maximum heat content. For Lake Superior the minimum and maximum heat contents around April 1st and October 1st respectively. The spring heat income for Lake Superior is about 1.5 x 10^9 Jm^{-2} and the annual heat income is about 2.4 x 10^9 Jm^{-2} (Titze 2013). Mid-lake upwelling of warm water in the winter tends to keep the central area free of ice and enhance heat loss (Bennett 1978).

Chapter 2

Mathematical background

2.1 Navier-Stokes Equations

The Navier-Stokes equations (honoring Claude-Louis Navier and George Gabriel Stokes) are a set of partial differential equations that define the motion of a parcel of fluid. Solutions to these equations define the velocity field at a particular time and point in space. The equations are derived from applying Newton's second law to a fluid parcel, see (Kundu and Cohen 2008) for a derivation. These equations are important in any situation that has fluid flow, such as modeling currents in the ocean or the dynamics of a aircraft. These equations were written down in the 19th century and are still relevant today in a practical and academic sense. In a rotating reference frame the Navier-Stokes equations are defined in vector notation as :

$$\rho(\frac{\partial \vec{V}}{\partial t} + \vec{\vec{V}} \bullet \nabla \vec{\vec{V}}) = -\nabla P - \rho(2\vec{\Omega} \times \vec{V}) - \rho \vec{g_n} - \rho \vec{\Omega} \times (\vec{\Omega} \times \vec{R}) + \mu \nabla^2 \vec{V} \tag{2.1}$$

Table 2.1: Definition of variables in the Navier-Stokes equations.

Term	**Description**
$\vec{V}$	Velocity vector : $\vec{V} = u\hat{x} + v\hat{y} + w\hat{z}$
$\vec{R}$	Displacement vector : $\vec{R} = x\hat{x} + y\hat{y} + z\hat{z}$
ρ	Fluid density
$\frac{\partial \vec{V}}{\partial t}$	Acceleration of fluid parcel
$\vec{V} \bullet \nabla\vec{V}$	Convective acceleration
∇P	Pressure gradient
$2\vec{\Omega} \times \vec{V})$	Coriolis acceleration
$\vec{\Omega} \times (\vec{\Omega} \times \vec{r})$	Centrifugal acceleration
$\mu\nabla^2\vec{V}$	Shear stress
$\vec{g_n}$	Newtonian gravitational acceleration
Ω	Rotation rate of Earth

The reference frame is oriented so positive x is to the east, positive y is to the north, and positive z is upward and pointing away from the surface of the Earth. Two terms in this expression arise because observations are made from a rotating (non-inertial) reference frame, the Coriolis acceleration (honoring Gaspard-Gustave Coriolis) $(2\vec{\Omega}\times\vec{V})$ and the centrifugal acceleration (Latin for "center fleeing") $(\vec{\Omega}\times(\vec{\Omega}\times\vec{R}))$. Keep in mind that these are not "real" accelerations in the sense that we can not name a force that is causing them, it is more appropriate to think of these as apparent accelerations that arise due to our frame of reference. The centrifugal acceleration is an apparent acceleration that is evoked in a non-inertial (accelerating) reference frame, which is opposite to the centripetal (center seeking) acceleration. To simplify the Navier-Stokes equation the centrifugal acceleration vector can be added to gravitational acceleration vector to define an affective gravitational acceleration $(-\vec{g} = -\vec{g_n} - \vec{\Omega} \times (\vec{\Omega} \times \vec{R}))$. The Coriolis acceleration gives rise to an apparent deflection of an object when it is moving; this deflection is clockwise in the northern hemisphere and counter-clockwise in the southern hemisphere. The components of the Coriolis acceleration are defined as :

$$2\vec{\Omega} \times \vec{V} = 2\Omega\sin(\phi)v\hat{x} - 2\Omega\sin(\phi)u\hat{y} \tag{2.2}$$

$$= -fv\hat{x} + fu\hat{y} \tag{2.3}$$

where $f = 2\Omega\sin(\phi)$ is the Coriolis frequency, $\Omega = \frac{2\pi}{\text{day}}$ is the rotational frequency of Earth and ϕ is latitude. The Coriolis period is given by $T = \frac{2\pi}{f}$. In Duluth, Minnesota (46.7°), located at the tip of Lake Superior's western arm, $f \approx 1.1 * 10^{-4}\text{s}^{-1}$ and the Coriolis period is $T \approx 16$ hrs. The physical meaning to the Coriolis frequency will be discussed in the next section.

Shear stresses, such as molecular friction ($\nu\nabla^2\vec{V}$), produce rotational motion which can be assumed negligible, at least in the ocean. The relative of importance of this term in the Navier-Stokes equation can be quantified by the Reynolds number, a dimensionless number defined as the ratio of inertial forces to viscous forces :

$$Re = \frac{UL}{\nu} \tag{2.4}$$

where U is a typical flow speed, L is typical length scale, and ν is the kinetic viscosity. A typical Reynolds value for open water in Lake Superior is $Re = \frac{(0.05\ ms^{-1})2*10^2m}{1m^2s} = 10^8$, a large Reynolds number implies that molecular friction can be neglected in the Navier-Stokes equation. Lastly, the local acceleration and advective acceleration can lumped into one term, the total acceleration, ($\frac{d\vec{V}}{dt} = \frac{\partial\vec{V}}{\partial t} - \vec{\vec{V}} \bullet \nabla\vec{V}$). After all of these simplifications the Navier-Stokes equation is reduced to :

$$\rho\frac{d\vec{V}}{dt} = -\nabla P - \rho(2\vec{\Omega} \times \vec{V}) - \rho\vec{g} \tag{2.5}$$

This equation will from hence force be referred to as the Navier-Stokes equation.

2.2 Pure Inertial Oscillations

Lets consider a parcel of water which is only affected by Coriolis force. In this case we can neglect the pressure term and gravitational term in the Navier-Stokes equation, since there will be no displacement of the surface and therefore no pressure gradients. The Navier-Stokes equations can then be written in vector notation as :

$$\frac{d\vec{V}}{dt} = -(2\vec{\Omega} \times \vec{V}) \tag{2.6}$$

$$\frac{du}{dt}\hat{x} + \frac{dv}{dt}\hat{y} = fv\hat{x} - fu\hat{y} \tag{2.7}$$

The component form of equation (2.7) is :

$$\frac{du}{dt} - fv = 0 \tag{2.8}$$

$$\frac{dv}{dt} + fu = 0 \tag{2.9}$$

where f is the Coriolis frequency, u is the zonal (east-west) component of the velocity and v is the meridional (north-south) component of velocity. Equation (2.8) is the x component and equation (2.9) is the y component. These coupled differential equations can be solved for $u(t)$ and $v(t)$ in the following way :

$$\frac{d^2u}{dt^2} - f\frac{dv}{dt} = 0 \tag{2.10}$$

We know that $\frac{dv}{dt} + fu = 0$ which implies that $\frac{dv}{dt} = -fu$, this can substituted equation (2.10).

$$\frac{d^2u}{dt^2} - f\frac{dv}{dt} = 0 \tag{2.11}$$

$$\frac{d^2u}{dt^2} + f^2u = 0 \tag{2.12}$$

$$\frac{d^2u}{dt^2} = -f^2u \tag{2.13}$$

We now have a second order ordinary differential equation whose general solution is $u(t) = u_o \cos(ft + \phi)$, where u_o is the initial zonal velocity and ϕ is the phase shift. This expression can be substituted into equation (2.8) to obtain an expression for $v(t)$.

$$\frac{du}{dt} - fv = 0 \tag{2.14}$$

$$\frac{d}{dt}(u_o \cos(ft + \phi)) = fv \tag{2.15}$$

$$-u_o f \sin(ft + \phi) = fv \tag{2.16}$$

$$-u_o \sin(ft + \phi) = v \tag{2.17}$$

The velocity field is given by :

$$u(t) = u_o \cos(ft + \phi) \tag{2.18}$$

$$v(t) = -u_o \sin(ft + \phi) \tag{2.19}$$

These equations can integrated over time to obtain expressions for the equations of motion :

$$x(t) = \int_0^t u(t')dt' = \int_0^t u_o \cos(ft' + \phi)dt' = \frac{u_o}{f} \sin(ft + \phi) \tag{2.20}$$

$$y(t) = \int_0^t v(t')dt' = \int_0^t -u_o \sin(ft' + \phi)dt' = \frac{u_o}{f} \cos(ft + \phi) \tag{2.21}$$

Physically these equations define a parcel of water moving in a circle of radius $\frac{u_o}{f}$ at a frequency f. The Coriolis frequency, occasionally called the Coriolis parameter, represents the angular frequency of an object acted on solely by the Coriolis force. This frequency is dependent on latitude, $f = 0$ at the equator and attains a max value at each pole. However, this situation neglects movement at the surface and corresponds to a wave having an infinite wavelength and therefore does not represent anything physical. Also notice that magnitude of the current does not change with time, which implies that Coriolis force acts perpendicular to the velocity vector and only acts to change the direction of motion but not the speed. A simple proof of this is provided below.

$$u(t) = \sqrt{u^2 + v^2} \tag{2.22}$$

$$= \sqrt{u_o^2 \cos(ft + \phi)^2 + -u_o^2 \sin(ft + \phi^2} \tag{2.23}$$

$$= \sqrt{u_0^2(\cos(ft + \phi)^2 + \sin(ft + \phi)^2)} \tag{2.24}$$

$$= u_o \tag{2.25}$$

This shows that the speed of the fluid parcel does not depend on time.

2.3 Poincaré Waves - Single Layer

This time we will allow the surface to move. A diagram of relevant variables is provided below.

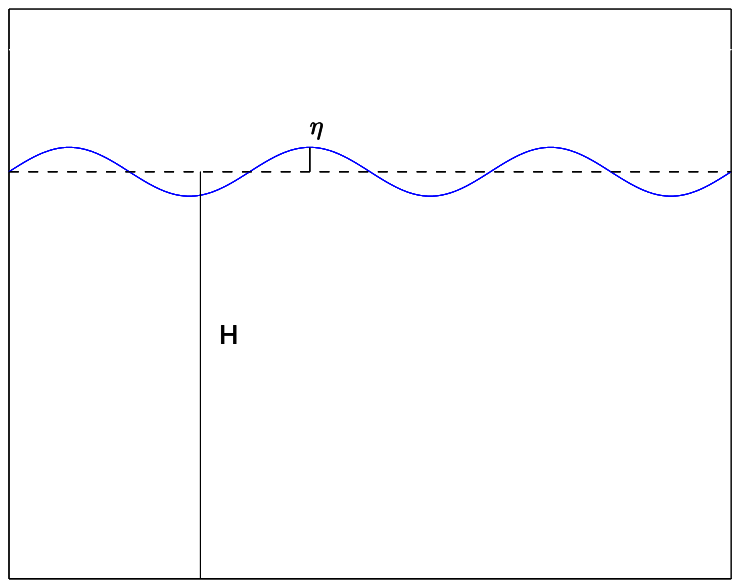

Figure 2.1: **single-layer-diagram.** H represents the depth of the water and and η represents the surface elevation from equilibrium

The Navier-Stokes equation for this situation can be written as :

$$\rho \frac{d\vec{V}}{dt} = -\nabla P - \rho(2\vec{\Omega} \times \vec{V}) - \rho\vec{g} \tag{2.26}$$

Lets substitute $\nabla P = \nabla \rho g \eta$ into the latter equation.

$$\rho\frac{d\vec{V}}{dt} = -\nabla P - \rho(2\vec{\Omega}\times\vec{V}) - \rho\vec{g} \tag{2.27}$$

$$\rho\frac{d\vec{V}}{dt} = -\rho g\nabla\eta - \rho(2\vec{\Omega}\times\vec{V}) - \rho\vec{g} \tag{2.28}$$

$$\frac{d\vec{V}}{dt} = -g\nabla\eta - (2\vec{\Omega}\times\vec{u}) - \vec{g} \tag{2.29}$$

$$\frac{du}{dt}\hat{x} + \frac{dv}{dt}\hat{y} + \frac{dw}{dt} = -g\frac{d\eta}{dx}\hat{x} - g\frac{d\eta}{dy}\hat{y} - g\frac{d\eta}{dy}\hat{z} + fv\hat{x} - fu\hat{y} - g\hat{z} \tag{2.30}$$

Separating the components we can write these equations as.

$$\frac{du}{dt} - fv = -g\frac{d\eta}{dx} \tag{2.31}$$

$$\frac{dv}{dt} + fu = -g\frac{d\eta}{dy} \tag{2.32}$$

$$\frac{dw}{dt} + g = -g\frac{d\eta}{dz} \tag{2.33}$$

The three equations can not be solved on there own since there are four unknown, $u, v, w,$ and η, therefore, the continuity equation needs to be included :

$$h(\frac{du}{dx} + \frac{dv}{dy}) + \frac{d\eta}{dt} = 0 \tag{2.34}$$

A plane wave solution of the following form will be applied to equations (2.31) - (2.34) :

$$(u, v, \eta) \sim (u_o, v_o, \eta_o)\exp i(\vec{K}\bullet\vec{R} - \omega t) \tag{2.35}$$

The wave vector, or vector extension of the wave number, can be written as $\vec{K} = [k_x; k_y; k_z]$. Without loss of generality we will assume the wave is solely propagating in the x direction. Applying a plane solution yields the following dispersion relation :

$$\omega^2 = f^2 + ghk^2 \tag{2.36}$$

This implies that f sets a lower limit to the frequency of a gravity wave.

Solving equations (2.31) - (2.34), (2.36) yields the following velocity field and surface elevation :

$$u(t) = \frac{\omega}{hk}\eta_o \cos(kx - \omega t) \tag{2.37}$$

$$v(t) = \frac{-f}{hk}\eta_o \sin(kx - \omega t) \tag{2.38}$$

$$\eta(t) = \eta_o \sin(kx - \omega t) \tag{2.39}$$

Since $\omega > f$ you will notice that $u > v$, which implies that the component of the speed is largest in the direction of propagation and that the parcels move in an ellipse instead of a circle.

The equations of motion can be found by integrating (2.37) and (2.38)

$$x(t) = -\frac{\omega}{hk}\eta_o(ku - \omega)\sin(kx - \omega t) \tag{2.40}$$

$$y(t) = \frac{-f}{hk}\eta_o(ku - \omega)\cos(kx - \omega t) \tag{2.41}$$

2.4 Poincaré Waves - Double Layer

Now lets consider a two layer fluid where a less fluid overlies a more dense fluid. The density of the fluid in each layer will be assumed constant throughout, i.e. pressure and temperature effects on density will be ignored. This scenario has two interfaces which can oscillate , the air-water interface and an internal interface separating the two fluid layers. The Navier-Stokes equation can be applied separately to each layer.

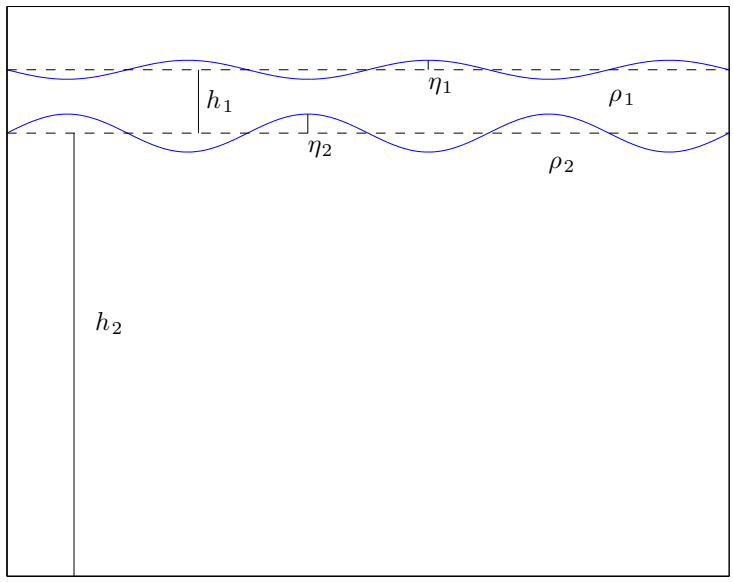

Figure 2.2: **two-layer-diagram.** h_1 will be the depth of the top layer and h_2 will be the depth of the bottom layer. The densities in each layer are given by ρ_1 and ρ_2, where $\rho_2 > \rho_1$. The interface displacements are given by η_1 and η_2 where $\eta_2 >> \eta_1$.

Top Layer

$$\frac{du_1}{dt} - fv_1 = -g\frac{d\eta_1}{dx}$$
$$\frac{dv_1}{dt} + fu_1 = -g\frac{d\eta_1}{dy}$$
$$h_1(\frac{du_1}{dx} + \frac{dv_1}{dy}) + \frac{d\eta_1}{dt} - \frac{d\eta_2}{dt} = 0$$

Bottom Layer

$$\frac{du_2}{dt} - fv_2 = -g'\frac{d\eta_2}{dx} - g\frac{d\eta_1}{dx}$$
$$\frac{dv_2}{dt} + fu_2 = -g'\frac{d\eta_2}{dy} - g\frac{d\eta_1}{dy}$$
$$h_2(\frac{du_1}{dx} + \frac{dv_1}{dy}) + \frac{d\eta_2}{dt} = 0$$

Solutions to these expressions are provided below.

$$u_1 = u_{10}\cos(kx - \omega t)$$
$$v_1 = \frac{f}{\omega}u_{10}\sin(kx - \omega t)$$

$$u_2 = -\frac{h_1}{h_2}u_{10}\cos(kx - \omega t)$$
$$v_2 = -\frac{h_1}{h_2}\frac{f}{w}u_{10}\sin(kx - \omega t)$$
$$\eta_2 = -\frac{h_1 k}{\omega}u_{10}\cos(kx - \omega t)$$

A rigid lid approximation was assumed which neglects variations of the air-water interface and assumes that surface behaves as an immobile surface or a "rigid lid."

Applying the same plane wave solution as in equation (2.35) to this two layer system yields the following dispersion relations.

$$\omega_{BT}^2 = f^2 + gHk^2$$
$$\omega_{BC}^2 = f^2 + g'h'k^2, \quad \text{where} \quad g' = g\frac{\Delta\rho}{\rho_o}, \quad h' = \frac{h_1 h_2}{H}$$

Since there are two layers there are two modes of oscillation, one which is depth independent and one which is depth dependent. The barotropic mode, ω_{BT}^2, is the depth independent mode and corresponds to the two layers moving in phase which each other. The system behaves as a homogenous fluid, as if there is no internal interface. The depth dependent mode, or baroclinic mode ω_{BC}^2, corresponds to the two interfaces moving out of phase with each other. When the surface layer is depressed the bottom layer is at its peak.

The Rossby radius of deformation defines a length scale when Earth's rotation becomes important. The Rossby radius is defined as the ratio of the wave speed to the Coriolis frequency. The Rossby radius of deformation defines the length scale at which rotation affects barotropic frequencies and the internal Rossby radius defines when rotation affects baroclinc frequencies. These values are quantified below assuming $\frac{\Delta\rho}{\rho_o} = \frac{1 \text{ kgm}^{-3}}{1000 \text{ kgm}^{-3}} = 0.001$ and $h' = \frac{h_1 h_2}{H} = \frac{20m130m}{150m} = 17.3$ m.

Rossby Radius

$$\begin{aligned} Re_e &= \frac{C}{f} \\ &= \frac{\sqrt{gH}}{f} \\ &= \frac{\sqrt{9.8\text{ms}^{-2}150\text{m}}}{1.1 * 10^{-4}\text{s}^{-1}} \\ &= 350 \text{ km} \end{aligned}$$

Internal Rossby Radius

$$\begin{aligned} Re_i &= \frac{C}{f} \\ &= \frac{\sqrt{g'h'}}{f} \\ &= \frac{\sqrt{9.8\text{ms}^{-2} * 0.001 * 17.3\text{m}}}{1.1 * 10^{-4}\text{s}^{-1}} \\ &= 4 \text{ km} \end{aligned}$$

Since the Rossby radius is comparable to the length scale of the Lake Superior basin (250 km), which means the barotropic signal will be weak. This can be shown by looking a spectrum of water levels in Lake Superior near Duluth, Minnesota. Conversely, the internal Rossby radius is much smaller than the length scale of Lake Superior suggesting

that these wave will be dominated by a baroclinic mode and be readily observable in current and temperature profiles.

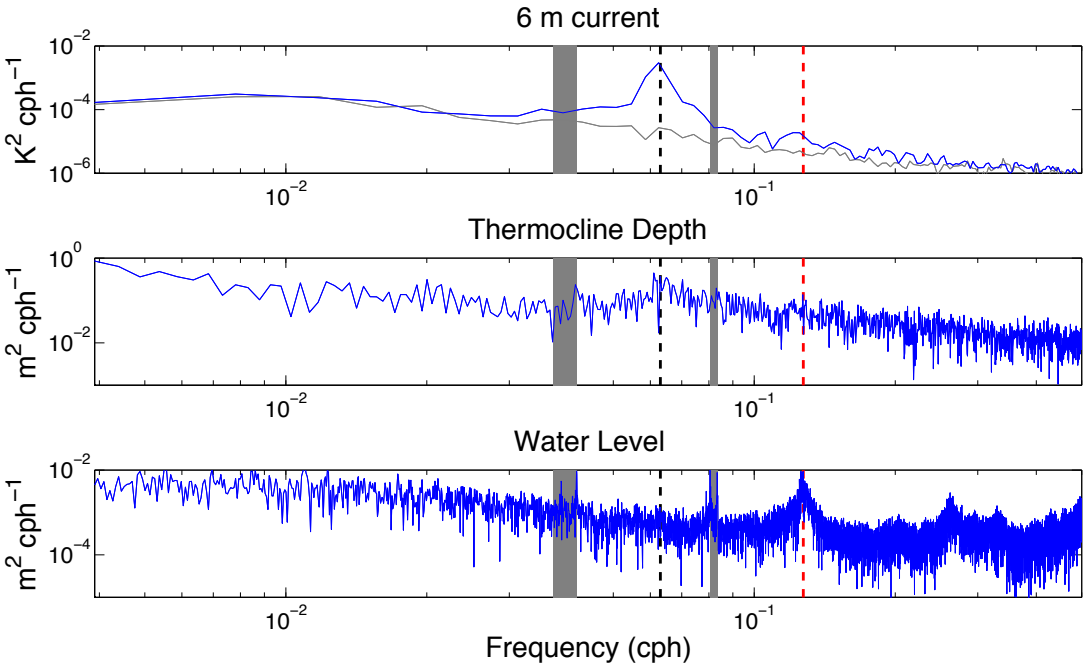

Figure 2.3: **Observational Spectrums.** This shows spectra from from observations of surface currents, temperature, and water levels during the 2011 field year. The black dotted line is at the local Coriolis frequency, the red dotted line is at the first seiche frequency and gray bars are the diurnal and semi-diurnal tidal bands.

This shows there is a significant amount of inertial energy observed in surface currents and thermocline undulations. However, there is weak inertial energy above background in water level records which suggests a weak barotropic response in Lake Superior and also gives justification for rigid lid approximation.

Chapter 3

Methods

3.1 Modeling

3.1.1 Configuration

ROMS is a three-dimension, free-surface, terrain-following numerical model that solves the Reynolds-averaged (time-averaged) Navier-Stokes equations using the hydrostatic and Boussinesq assumptions. The hydrostatic assumption assumes the vertical pressure force is balanced by the weight of the fluid parcel. In which case, the pressure at a given depth is given by the hydrostatic equation, $\frac{\partial P}{dz} = -\rho g$. The Boussinesq approximation assumes that density variations are negligible in the Navier-Stokes equations, except for the buoyancy term where ρ is multiplied by g. The non-linear equations of motion are solved using a predictor(leap-frog)-corrector(Adam-Molten) finite difference scheme. To solely look at the affects of surface stress and stratification on near-inertial energy the model was configured for no radiative forcing. Without radiative forcing the heat content of the water column can not change and stratification can not form on its own.

Lake Superior was modeled as closed basin with no inflows or outflows. The bathymetry used has a spatial resolution of 2km (Schwab and Sellers 1996) and was smoothed with the following three point moving average :

$$x_t = 0.25x_{t-1} + 0.5x_t + 0.25x_{t+1} \tag{3.1}$$

until the Beckman and Haidvogel number was less than 0.4. A small Beckman and

Haidvogel number ensure model stability and avoids spurious deep water currents. This number is defined as :

$$R_x = \max \frac{|h(i) - h(j)|}{h(i) + h(j)} \tag{3.2}$$

where $h(i)$ and $h(j)$ is the depth at neighboring grid cells and R_x is the Beckman and Haidvogel number.

Lake Superior spans about 2.5 degrees of latitude, the Coriolis parameter over this range changes by about 3%. Because the change in the Coriolis parameter is small the model configured using an f-plane approximation. The Mellor-Yamada closure scheme was used in the model, which takes eddy viscosity into account and estimates turbulence on scales which can not be resolved by the model. Model output was linearly interpolated onto a common grid. One implication of this is current velocities one grid cell away from the coast must be discarded since the interpolation used points outside the basin. A diagram of a grid cell is provided below.

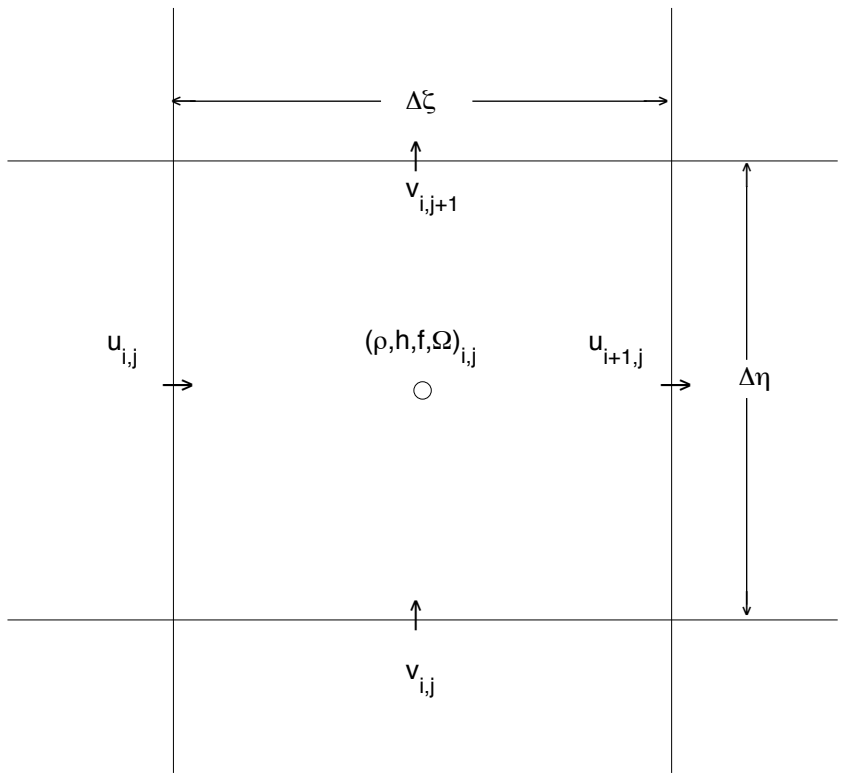

Figure 3.1: **Arakawa-C Grid Cell.** The Arakawa-C grid cell computes density, depth, and Coriolis frequency at the center of each cell. The u and v component of the velocity are computed half a cell distance away. $\Delta\eta$ and $\Delta\zeta$ are the resolution of the model in the meridional and zonal direction respectively.

The model used a time step of Δt =200 seconds and data was output hourly. The time step at the surface is $\frac{\Delta t}{30}$, since the waves evolve much faster at the surface. For stability, the CFL (Courant-Friedrichs-Lewy) condition requires the courant number to be less than 1 everywhere in the model. This condition can be expressed as $|\frac{V\Delta t}{\Delta x}| \leq 1$, where V is the maximum internal wave speed Δt is the internal time step and Δx is the horizontal spatial resolution. It is easy to show the CFL condition holds at the deepest point in the model (350 m) by calculating the courant number for a wave at the surface and at the internal interface.

External Courant Number

$$\frac{V_{external}\frac{\Delta t}{30}}{\Delta x}$$

$$\frac{\sqrt{gH_{max}}\frac{\Delta t}{30}}{\Delta x}$$

$$\frac{\sqrt{9.8ms^{-1}350m}\frac{200s}{30}}{2000m}$$

$$0.20 < 1$$

Internal Courtant Number

$$\frac{V_{internal}\Delta t}{\Delta x}$$

$$\frac{\sqrt{g'h'}\Delta t}{\Delta x}$$

$$\frac{\sqrt{9.8 * 0.001 * \frac{20m*330m}{350m}} * 200s}{2000m}$$

$$0.04 < 1$$

The model is likely to be stable since the courant number is always less than one. The purpose of the CFL condition is so we do not advect material through a grid cell in the given time step. Note that the CFL condition is required for model stability but is not sufficient and therefore will not guarantee a stable model. More information on model stability can be found in Glover et al. (2011).

3.1.2 Vertical Structure

The model was configured with 30 vertical layers staggered throughout the water column. The spacing between vertical levels varied from 0.2 m at the surface to 15 m at the bottom. The vertical stretching was given by :

$$C(\sigma) = \frac{1 - \cosh(\theta_s \sigma)}{\cosh(\theta_s) - 1} \tag{3.3}$$

where $\theta_s = 3$, $\sigma = \frac{k-N-0.5}{N}$ $\quad k = 1 \ldots N$, where N is the number of vertical layers.

Two types of thermal structures were used, a homogenous water column of uniform temperature and a stratified water column. The well mixed water column was chosen to be $4°C$ since it is close to T_{md}. However, it should be noted that any temperature could have been chosen and this temperature does affect the dynamics of the water column. Stratification was modeled as a two layer system, the modeled thermal structure was given by the following equation.

$$T(z) = T_{bot} + (\frac{T_{top} - T_{bot}}{2}) * (1 + \tanh(\frac{(z + z_{cline})}{s})) \tag{3.4}$$

Where T_{bot} is the temperature of the bottom layer, T_{top} is the temperature of the top layer, z_{cline} is the thermocline depth, and s is a steepness parameter for the gradient of the thermocline. The following values were used in the thermal structure equation.

Table 3.1: Thermal Stratification Values

Parameter	**Value**	**Description**
T_{bot}	$4°C$	Bottom layer temperature
T_{top}	21 $°C$	Top layer temperature
z_{cline}	20 m	Thermocline depth
s	2	Thermocline steepness parameter

A diagram of the initial thermal structure is shown below for a point in the model which has a depth of 160m.

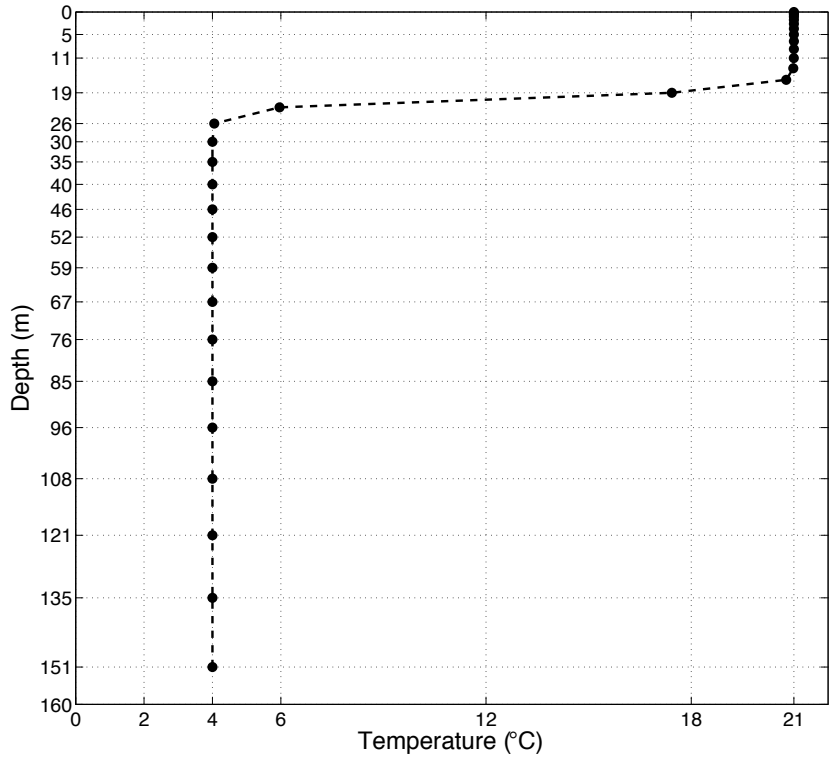

Figure 3.2: **Modeled Initial Thermal Structure.** Shows the initial thermal structure for a point where the max depth is 160m. This also shows the spacing in the model.

The spacing between grid cells decreases with depth. The spacing at the top is on the order of a meter while at the bottom it is on the order of 20 m. One downside to this thermal structure is only about three or four temperature readings are taken in the metalimnion so the thermocline can not be highly resolved.

3.1.3 Forcing

Two types of forcing were used, an impulse of idealized wind stress and temporally and spatially varying wind stress. The idealized forcing was a spatially uniform pulse of wind stress with a magnitude of 0.1 Nm^{-2}; this is equivalent to a wind speed of 8 ms^{-1} at 10m above the surface (Fairall et al. 1996). To maximize the energy input at the inertial frequency the duration of the wind pulse lasted for half an inertial period (Boyce

et al. 1989).

Temporally and spatially varying wind stress was derived from the North American Regional Reanalysis (NARR) climatology data. This is an extension of NCEP Global Reanalysis which runs models of the North American region. NARR provides high resolution (32km spatial / 45 layers) climatology model output from 1979 up to today with a temporal resolution of 3 hours. The zonal and meridional wind speeds at 10m above the surface from 2011 were used to compute the wind stress at the surface. The modeled wind stress was linearly interpolated to an hourly time grid and objective analysis was used to interpolate the output onto a 2km x 2km grid. To show the spatial variability in the wind stress snapshots of the wind stress derived from NARR climatology output are provided below.

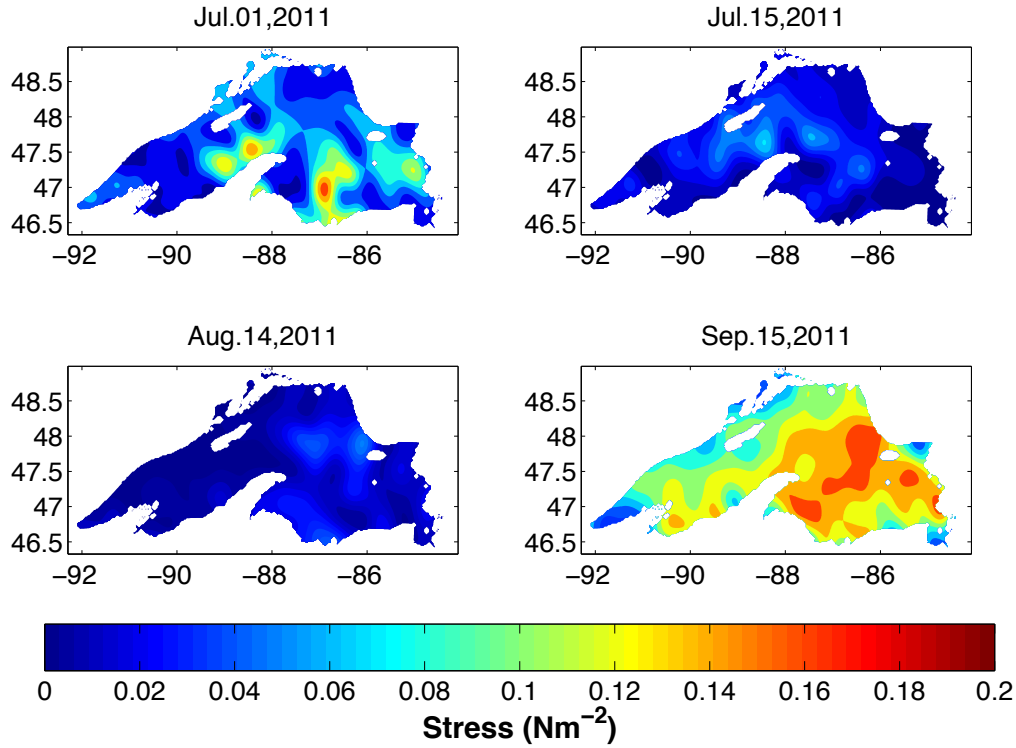

Figure 3.3: **NARR Stress.** Snapshots of the wind stress

The surface stress computed from NARR was compared to wind stress computed

from observed NDBC data. The NDBC wind stress appears coherent at the core mooring sites, however, the NARR stress does not completely capture all the features of the observed stress. There are also times when the two series are 180° out of phase. Plots of observed and modeled wind stress are provided below.

A comparison between each site is given below. The NARR stress follows the general shape of the observed NDBC stress but acts as a smoothed version of the observed data. In other words, the NARR stress does not follow of the extreme events.

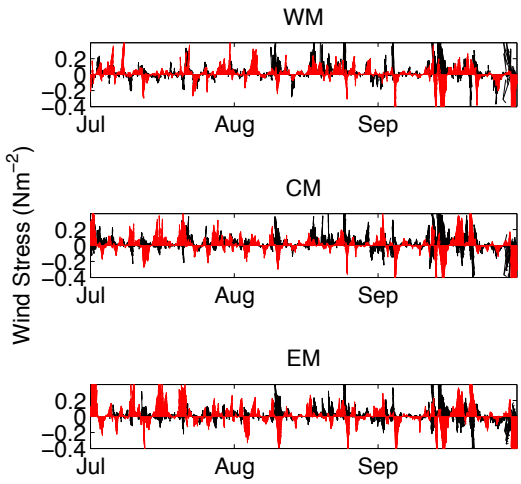

Figure 3.4: **Core Mooring Stress.** Compares observed wind stress at the core mooring sites to wind stress computed from NARR. The black arrow represents the observed (NDBC) data and the red arrows represent the NARR stress.

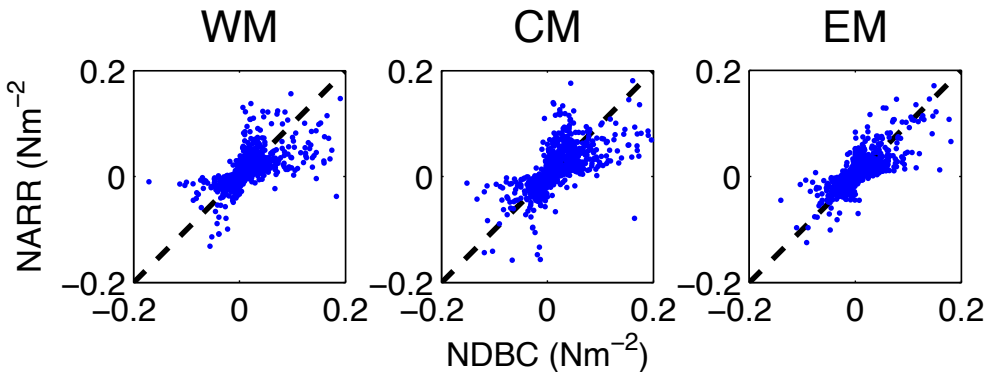

Figure 3.5: **NDBC vs NARR.** Wind stress derived from NDBC vs wind stress derived from NARR at each mooring location.

3.1.4 Computation

Computation was done at the Minnesota Supercomputing Institute (MSI) located on the Twin Cities campus of the University of Minnesota. The model was partitioned into 16 equal pieces each computed on different computing nodes on MSI's Calhoun cluster. Calhoun is an SGI Altix XE 1300 Linux cluster with 180 SGI Altix XE 300 computing nodes. Each node contains two quad-core 2.66 GHz Intel Xeon processors sharing 16 GB of memory. In total, Calhoun consists of 1440 computing cores and 2.8 TiB of main memory. A model run of 90 days and outputting every hour would takes approximately 16 hours to complete using 16 processors.

3.2 Lake Superior Mooring Array

The Lake Superior mooring array is a collection of up to seven moorings which have been continuously deployed since 2005. In 2005 the Western Mooring (WM) was deployed and was the only mooring for three years. The Eastern (EM) and Central (CM) Moorings were included in the array in 2008. These three moorings form the "core mooring" array which is still in operation today. The core moorings locations were chosen to be with 1 to 2 km of National Data Buoy Center (NDBC) buoys. with the WM, CM, and EM locations coinciding with NDBC buoys 45006, 45001, and 45004, respectively. To increase spatial variability four more moorings have included, these are the Far Western

(FWM); Northern (NM); Southern (SM); and Far Eastern Moorings (FEM). However, these supplemental moorings were only in operation from 2008 to 2012. The moorings remain in continuous operation once deployed but are removed once or twice a year to replace batteries and retrieve data.

Instruments on the moorings have included thermistor strings, Acoustic Doppler Current Profilers (ADCP) (Bugnon and Whitehouse 1991), ice profilers, O_2 sensors, NO_3 sensors, and sediments traps. However, this thesis will only discuss thermistor and ADCP data sets.

Each mooring is equipped with 10 to 13 thermistors irregularly spaced throughout the water column. Thermistors are spaced closer together near the surface to capture the abrupt temperature change in the thermocline during the stratified season and coarsely spaced near the bottom where the temperature remains relatively constant throughout the year. Due to coast guard restrictions, thermistors extend 7 to 10 meters below the water surface. The coincident NDBC buoy can be used to fill in the temperature gap near the surface, since they record temperature at 1 m depth. The anchor and acoustic release limit the bottom thermistor to a depth of 3 to m meters above the lake bed.

A few different thermistor models have included on the moorings, including Brancker Research (RBR) TR-1000, TR-1050, TR-1060, and TD-2050 sensors, and Seabird Electronics SBE-39 and SBE-39P sensors. Each thermidor is deployed with a pressure sensor to verify the depth. The storage capacity of the instruments limits the sampling rate, with the TR-1000 and SBE sensors taking measurements every 10 minutes, and the TR-1050, TR-1060, and TD-2050 sensors taking measurements every 1 minute

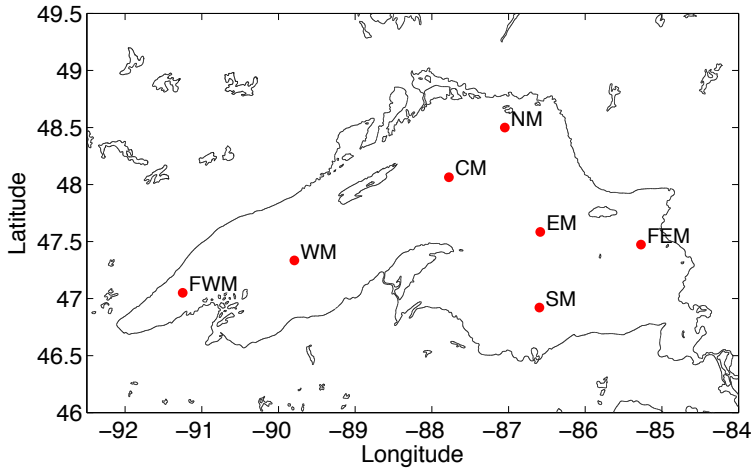

Figure 3.6: **Lake Superior Mooring Array.** Locations of active and inactive moorings in Lake Superior deployed since 2005

Table 3.2: Mooring Array

Mooring Name	Latitude	Longtidue	Depth (m)
Western Mooring (WM)	47° 19.018’	89° 48.520’	185
Central Mooring (CM)	48° 1.384’	87° 46.006’	255
Eastern Mooring (EM)	47° 32.186’	86° 34.261’	213
Far Western Mooring (FWM)	47° 3.005’	91° 14.928’	170
Northern Mooring (NM)	48° 29.972’	87° 2.935’	201
Southern Mooring (SM)	46° 55.252’	86° 35.805’	384
Far Eastern Mooring (FEM)	47° 28.375’	85° 16.394’	247

3.3 ADCP

ADCPs have been routinely placed with the core moorings and have been sporadically included in the FWM and NM. The ADCP sends out an acoustic pulse that reflects off particles moving passively with the current. The ADCP uses the reflected signal to determine the speed of the particle in the zonal and meridional direction. The ADCP

was programmed to make readings every 10m. Spurious reflections can occur from fish or other instruments on the mooring line. A record of ADCP deployments at the mooring sites is provided below.

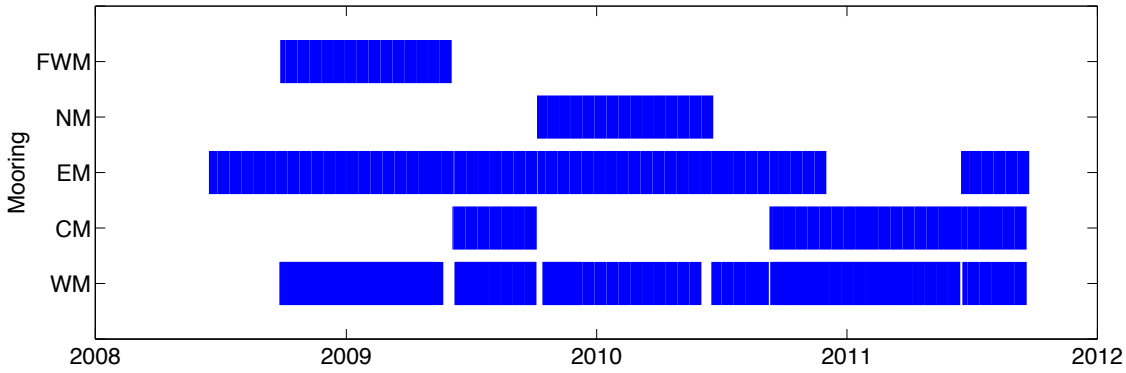

Figure 3.7: **ADCP Deployment Record.** Deployments of upward or downward looking ADCP at mooring sites.

3.4 Wavelet Analysis

Many geophysical time series have non-stationary statistics, i.e. the mean and variance change with time. A Fourier transform can be used to determine whether a frequency is present in a time series, however, a periodogram of the Fourier transform does not give any information about how the amplitude of each frequency varies with time. A simple way to deal with non-stationary time series is to compute a running variance and running mean, however, this contains no frequency information and is highly dependent on the length of the window. To gain information about the frequency of a periodic signal a running Fourier transform can be used. This involves using a certain window width and sliding it over the time series, computing the fast Fourier transform (FFT) at each time (using only the data inside the window). The problem with the latter is that at low frequencies can not be resolved since very few, if any, oscillations will fit inside the window. Also, at high frequencies there are so many oscillations in the window that the frequency is not localized in time. Wavelet analysis attempts to solve this time and frequency localization problem.

Wavelet analyses are used to study the temporal variability of power at many different frequencies. A wavelet is a function which has zero mean and is localized in time and frequency. Traditionally, wavelets from a spectrum of frequencies are convoluted with with a time series. This thesis will only use wavelets tuned to a specific frequency. Time series were convoluted using a clockwise and counter-clockwise rotating Morlet wavelet of the form:

$$w_{\pm}(t_0) = (\tau\sqrt{\pi})^{-1} e^{-(\frac{(t-t_0)}{\tau})^2} e^{\mp i\omega t} \tag{3.5}$$

where τ is window width, ω is the frequency of the wavelet, t is time vector, and t_0 is the central position in time of the wavelet. Power is determined using

$$P_{\pm}(t) = \int_{-\infty}^{\infty} w_{\pm} U \, \mathrm{d}t \tag{3.6}$$

where $U = u + iv$ is the complex velocity (u is the zonal component while v is the meridional component). The power yields informations about the magnitude and phase of the near-inertial waves. The complex Morlet wavelet is formed from the product of a Guassian curve and a sine or cosine function, Figure 3.8.

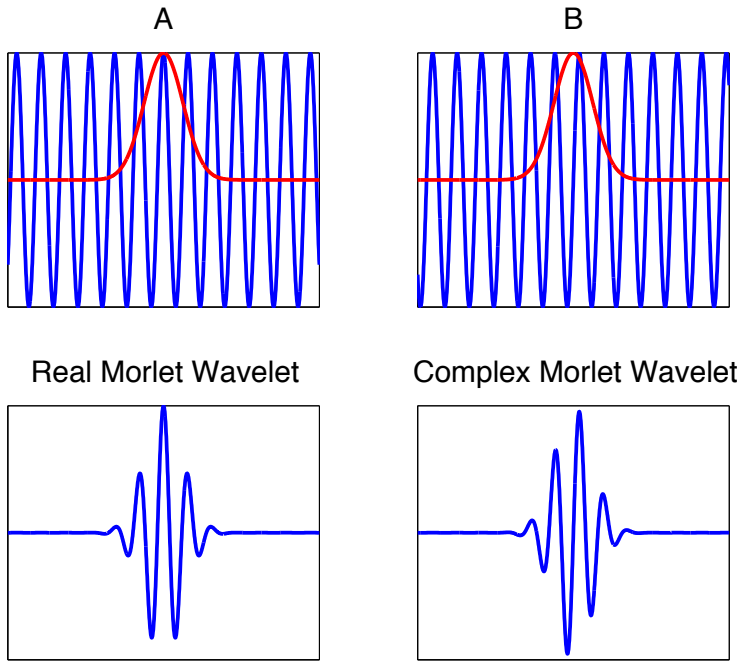

Figure 3.8: **Complex Morlet Wavelet.** Column A shows the product of a Gaussian curve and a cosine function and the column B shows the product of a Gaussian curve and a sine function. The bottom row shows the result of these products, which are the real and complex component of the Morlet wavelet.

3.5 Near-Inertial Energy

Energy in this motion is carried in vertical oscillations of the water column, primarily at the thermocline, which represents the potential energy or the currents associated with this motion which represents the kinetic energy. Since Lake Superior is a large Burger number lake a greater fraction of this energy is carried in potential energy (Antenucci and Imberger 2001).

3.5.1 Near-Inertial Potential Energy

Near-inertial potential energy is carried in undulations of pycnolines. The largest of these vertical migrations occur at the thermocline, therefore undulations of the thermocline are commonly used as an estimate of near-inertial potential energy. The vertical

stratification scale was estimated by the following equation:

$$z_s = \frac{\sum_{i=1}^{N} \frac{\Delta T_i}{\Delta z_i} z_{i,mid}}{\sum_{i=1}^{N} \frac{\Delta T_i}{\Delta z_i}}$$

where z_{mid} is the mid point between adjacent grid cell, ΔT_i is the temperature difference of the adjacent grid cells, and Δz_i is the distance between each vertical grid cell.

3.5.2 Integrated Kinetic Energy

The classical expression for kinetic energy can be used to estimate the kinetic energy of a fluid column :

$$\begin{aligned} KE &= \sum \frac{1}{2} v_i^2 \Delta m_i \\ &= \frac{1}{2} \sum \rho_i A v_i^2 \Delta z_i \end{aligned}$$

Where m_i is the mass of each parcel of fluid, v_i is the speed of the current at each depth i, A is the surface area of each parcel, and Δz_i is the thickness of each layer. If the surface area of each parcel is a constant then we can write the kinetic energy per area :

$$\frac{KE}{A} = \frac{1}{2} \sum \rho_i v_i^2 \Delta z_i$$

Given raw velocity this expression will not tell us anything about energy at the inertial frequency. In order to establish kinetic energy at the inertial frequency a measure for the inertial velocity needs to be established. Wavelet analysis and the rotary spectrum can be used to isolate the inertial velocity. The amplitude of a wavelet tuned to the inertial frequency can be used as an estimator of the inertial velocity. This method has the advantage of looking at temporal variations of inertial energy. Another method to estimate inertial velocity is to use the rotary spectrum of the current at each depth and then pick value of the clockwise component at the inertial frequency. The units of this value (assuming frequency in cycles per hour) will be $m^2 s^{-2} cph^{-1}$ which is proportional to the inertial velocity. To transform this value into a current you need to divide by the

inertial frequency and then take the square root. The latter method can be enhanced to accommodate to a range of frequencies, in which case you would integrate under the range of frequencies and then take the square root. This method takes into account the entire time series and therefor you lose information about time, but this method has the advantage of defining one number for the inertial velocity. This thesis will use the wavelet method to estimate the inertial velocity since it provided temporal information. To speed up computation time I will assume the inertial energy energy at the surface is representative of the total integrated kinetic energy. This can be justified since most of the kinetic energy is in the top mixed layer while weak currents are present below the thermocline. The kinetic energy will also be weighted by the water depth at each point to take into account bathymetric effects. The expression below was used to estimate near-inertial kinetic energy :

$$\frac{KE}{V} = \frac{\frac{1}{2}\rho_{surf} v_{surf}^2 \Delta z_{surf}}{H}$$

Where ρ_{surf} is the water density at the surface, v is the inertial velocity estimated from the amplitude of the clockwise wavelet at Coriolis frequency, Δz_{surf} is the depth at which the velocity measurement was taken, and H is the water depth .

Chapter 4

Results

4.1 Modeling

A hierarchy of models were used to explore the effects of wind duration, curl in the wind field, and bathymetry on the spatial distribution of near-inertial energy. Three basins were considered, an ideal flat bottom basin, a flat bottom basin with Lake Superior coastline, and a Lake Superior coastline with realistic bathymetry. Two thermal structures were explored, a homogenous thermal structure of 4°C and a two layer structure. Three types of forcing were used, a spatially uniform top-hat wind stress , a spatially uniform rotating wind stress, and spatially/temporally varying wind stress derived from NARR wind speeds.

4.1.1 Ideal Basin : Closed Boundaries

The ideal model was a 200km by 200km square basin with a uniform depth of 165 m. The model was forced with a spatially uniform top-hat wind stress with a magnitude of 0.1 Nm^{-2}. The thermal structure was a two layer system with the thermocline depth set to 20 m, the top layer $21°C$, and the bottom layer $4°C$.

The temperature contour for the ideal model is given below. Notice that the thermocline starts to oscillate after an internal wave has propagated 100 km.

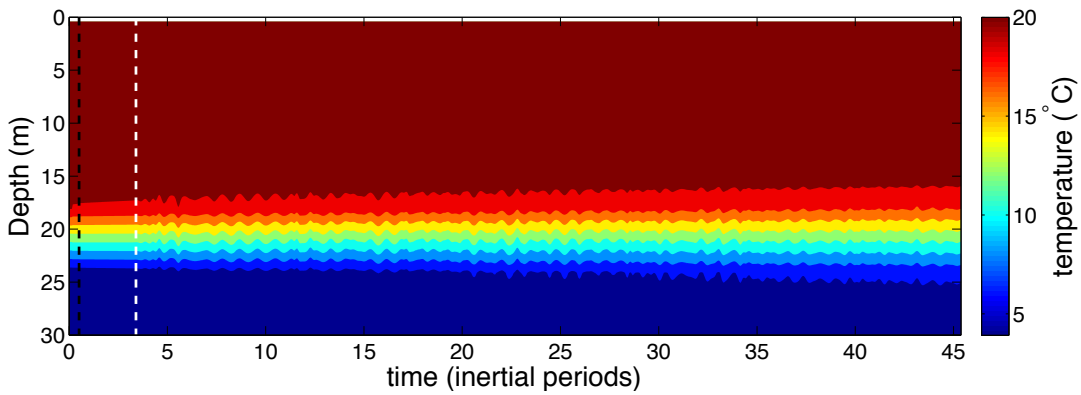

Figure 4.1: **Temperature Contour.** Temperature contour at the center of the ideal basin. The black dotted line is at 8 hours, the time forcing stops. The white dotted line is the time it takes an internal wave to propagate 100km, this was computed after the forcing had stopped. The x-axis is in units of inertial periods, where the inertial period if about 16 hours.

In order for undulations of the thermocline to begin surface must subside and push down the thermocline. This can happen at the coast where there is a boundary or when surface waves moving in opposite directions meet. The above plot shows that undulations of the thermocline at the center of the ideal model are not "felt" until the wave stating at the coast has reached that point. The times it takes this wave to reach this point is given by dividing the distance from by the internal wave speed ($t = \frac{d}{c_{int}}$). The white line in the plot shows this time after the surface stress has ceased. This time corresponds to when undulations begin. This suggests that a coast is necessary for thermocline undulations to persist.

The velocity contour at the center of the ideal basin is provided below.

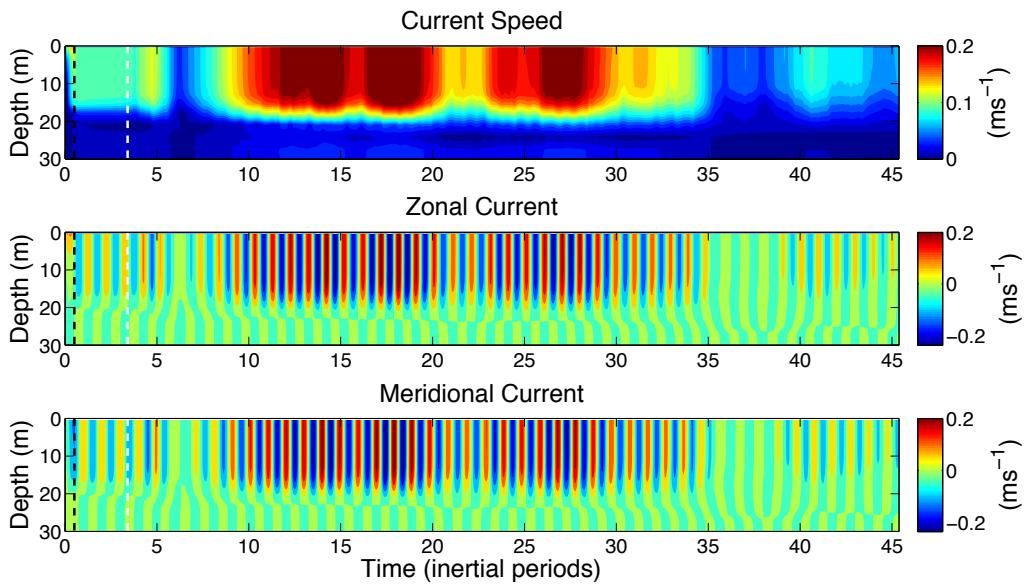

Figure 4.2: **Current Contour.** Current contour at the center of the ideal basin. The black dotted line is at 8 hours, the time forcing stops. The white dotted line is the time it takes an internal wave to propagate 100km, this was computed after the forcing had stopped. The x-axis is in units of inertial periods, where the inertial period if about 16 hours.

This shows a back and forth motion of the zonal and meridional velocity components. The current vector moves in clockwise fashion from north, to west, to south, to east in approximately one Coriolis period. High currents are observed above the thermocline with weaker currents below. The clockwise and counter-clockwise wavelet

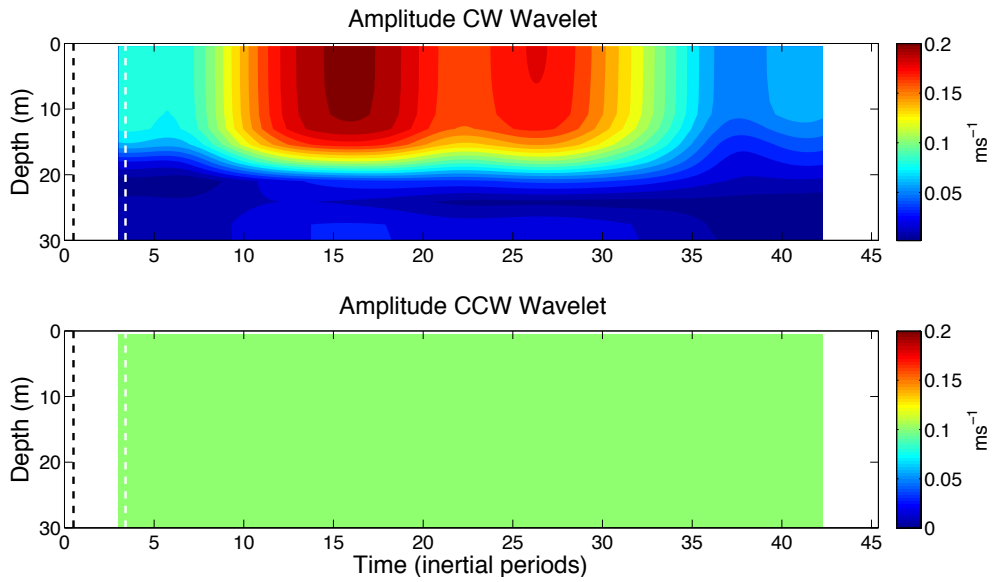

Figure 4.3: **Wavelet Contour.** Contour plot of clockwise and counter-clockwise wavelet amplitude at the center of the basin. The black dotted line is at 8 hours, the time forcing stops. The white dotted line is the time it takes an internal wave to propagate 100km, this was computed after the forcing had stopped. The x-axis is in units of inertial periods, where the inertial period if about 16 hours.

Spectral of surface currents, thermocline undulations, and the 18 m depth temperature are provided below. The surface currents show a significant amount of energy at the inertial frequency. Thermocline undulations and 18 m temperature show substantial energy in the super-inertial range. Interestingly, the peak in the thermocline spectrum and 18 m spectrum is shifted more into the super-inertial range than the peak in the surface current spectrum.

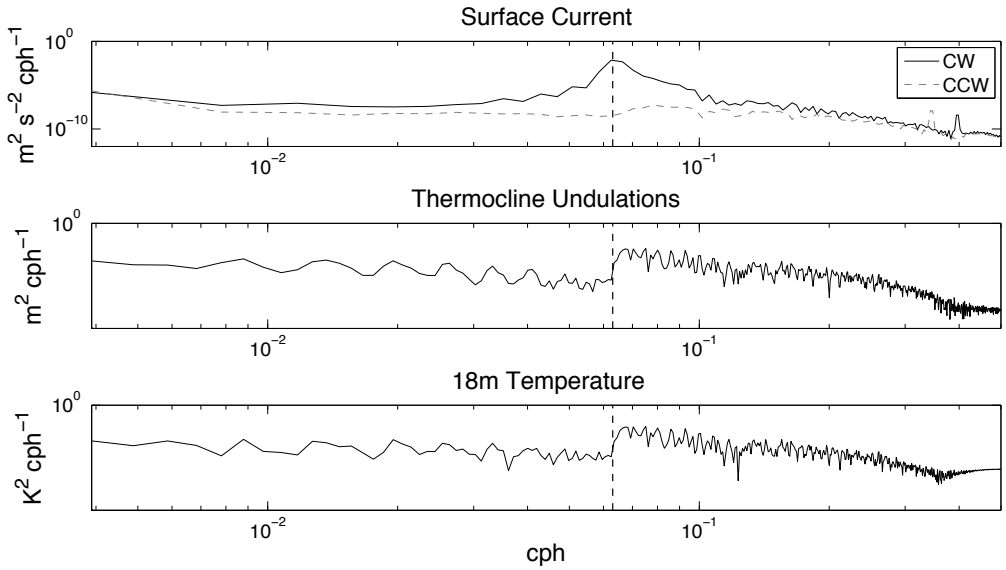

Figure 4.4: **Ideal Spectrums.** Spectrums from surface currents, thermocline undulations, and 18 m temperature. The black dotted line is at the inertial frequency.

Snapshots of the surface energy are provided below. The energy decreases at the coast and after about 150 hours most of the energy stay concentrated near the center of the basin.

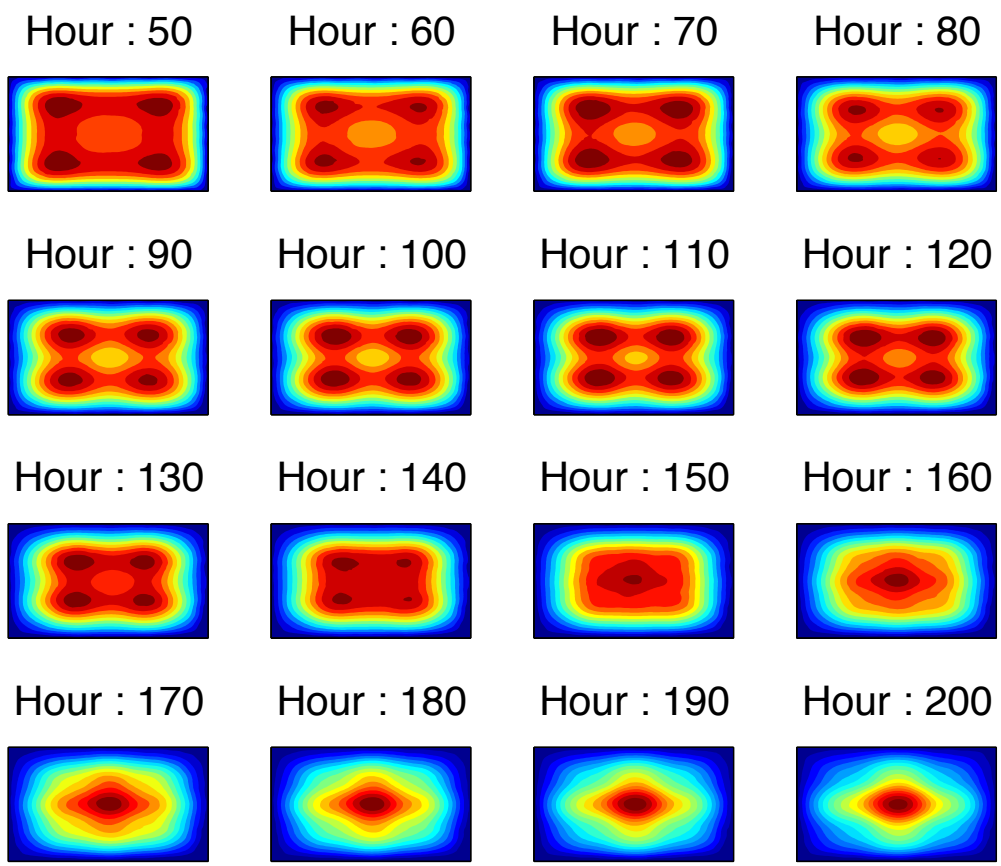

Figure 4.5: **Ideal Surface Energy.** Snapshots of surface energy in ideal basin.

4.1.2 Ideal Basin : Periodic Boundaries

A model with doubly periodic boundary conditions was ran. This model was useful to show that a coastline is necessary to start thermocline undulations. A contour plot of the temperature at the center of the basin is shown below.

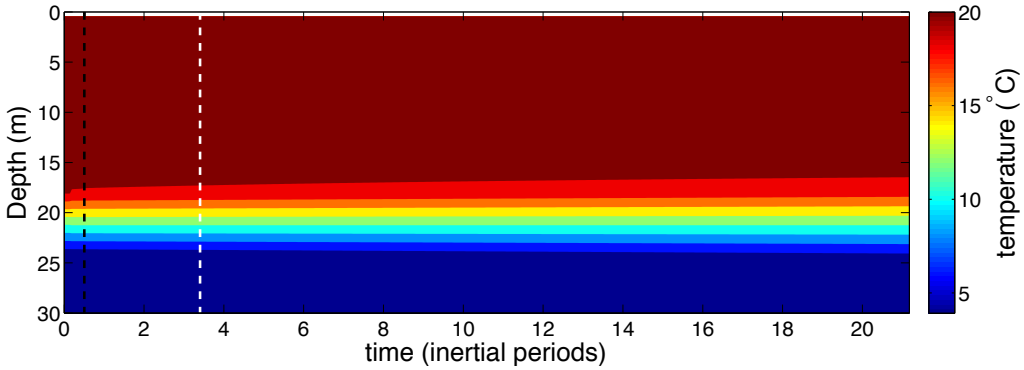

Figure 4.6: **Periodic Temperature Contour.** Temperature contour at the center of the ideal basin with periodic boundaries. The black dotted line is at 8 hours, the time forcing stops. The white dotted line is the time it takes an internal wave to propagate 100km, this was computed after the forcing had stopped. The x-axis is in units of inertial periods, where the inertial period if about 16 hours.

The current contour at the center of the model is provided below. Notice that there are high currents in the top mixed layer and no motion below the thermocline. The top layer shows pure inertial motion with the current vector rotating clockwise at the inertial frequency.

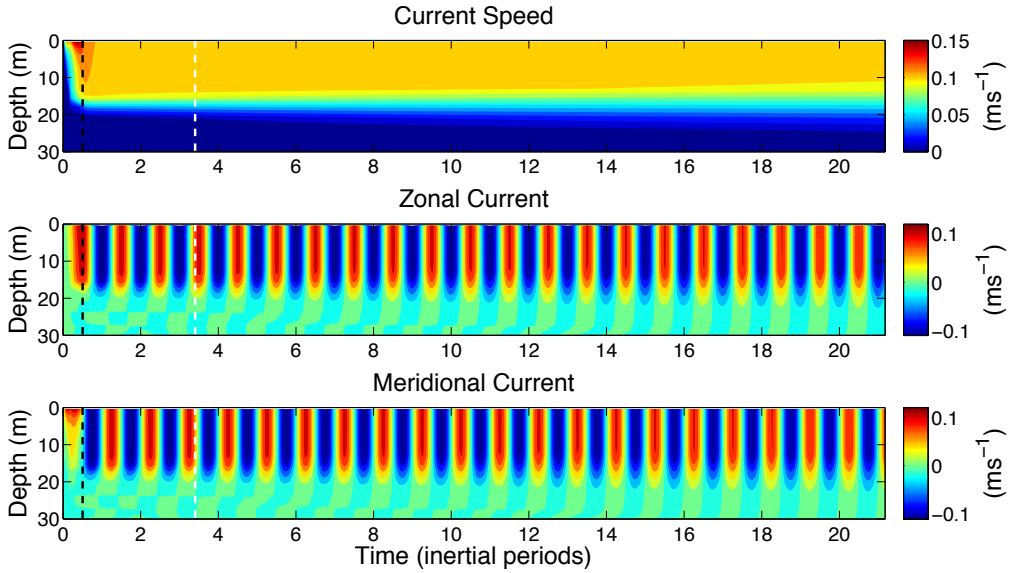

Figure 4.7: **Periodic Current Contour.** Current contour at center of ideal basin with periodic boundaries. The black dotted line is at 8 hours, the time forcing stops. The white dotted line is the time it takes an internal wave to propagate 100km, this was computed after the forcing had stopped. The x-axis is in units of inertial periods, where the inertial period if about 16 hours.

Spectral of surface currents, thermocline undulations, and the 18 m depth temperature are provided below. Notice there is no energy in the thermocline undulations and the peak in the current spectrum is centered at the inertial frequency. This is indicative of pure inertial motion, in other words all the inertial energy is kinetic energy.

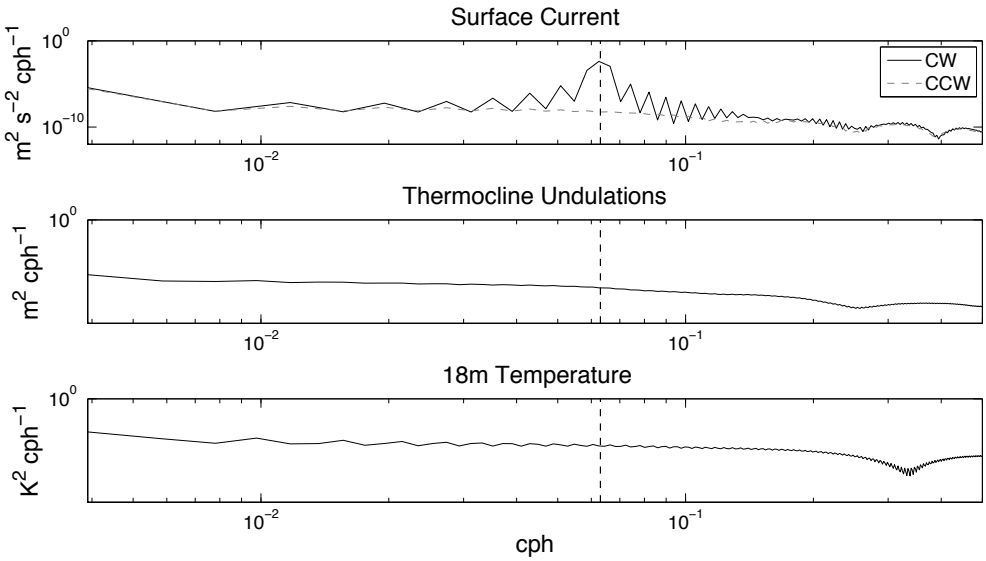

Figure 4.8: **Periodic Spectrum.** Spectrums from surface currents, thermocline undulations, and 18 m temperature. The black dotted line is at the inertial frequency.

4.1.3 Lake Superior : Flat Bottom

The flat bottom Lake Superior model was configured using 5km x 5km spatial resolution and a uniform depth of 165 m. The forcing used was a top-hat wind stress lasting for half an inertial period. To estimate the inertial energy across the basin a rotary spectrum was applied to the surface currents and the peak in the clockwise rotary spectrum at the inertial was used as an estimate for the inertial energy. The analysis shows high energy in the open lake and decreasing energy near the coast. A plot of the spatial distribution of energy is provided below.

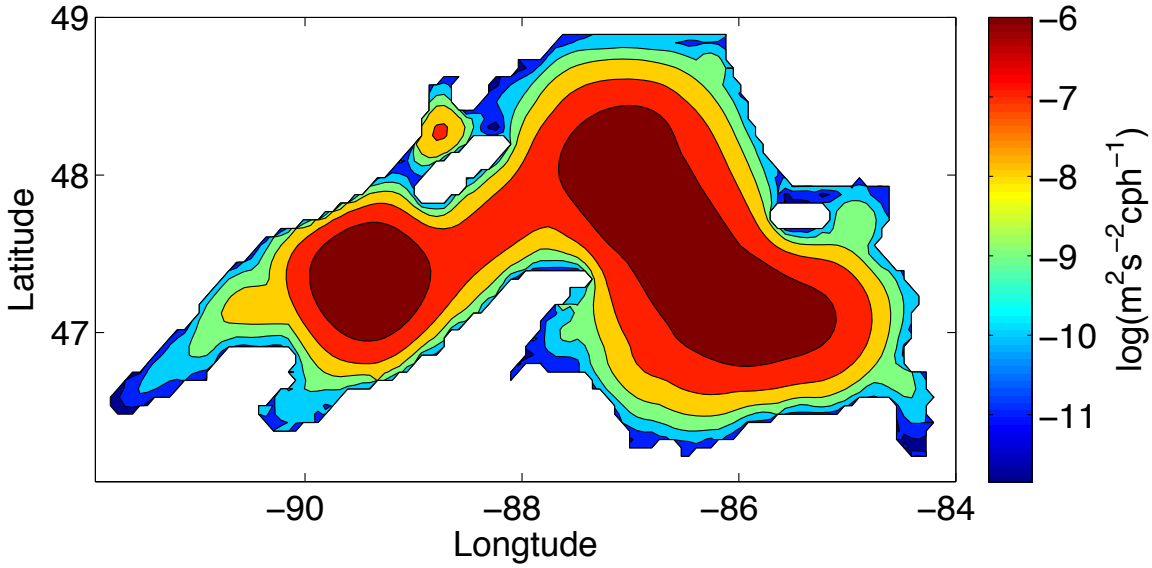

Figure 4.9: **Spatial Energy - Flat Bottom.** Peak in the clockwise rotary spectrum at the Coriolis frequency.

To be consistent, re-run this model using 2km x 2km spatial resolution.

4.1.4 Lake Superior : Realistic Bathymetry

The realistic bathymetry was 2km by 2km closed basin and was forced realistic wind stress derived from the 2011 NARR wind field. In order to compare modeled output with observational data stations were placed in the model at the approximate location of the core moorings. Below is a plot of the spatial distribution of surface kinetic energy.

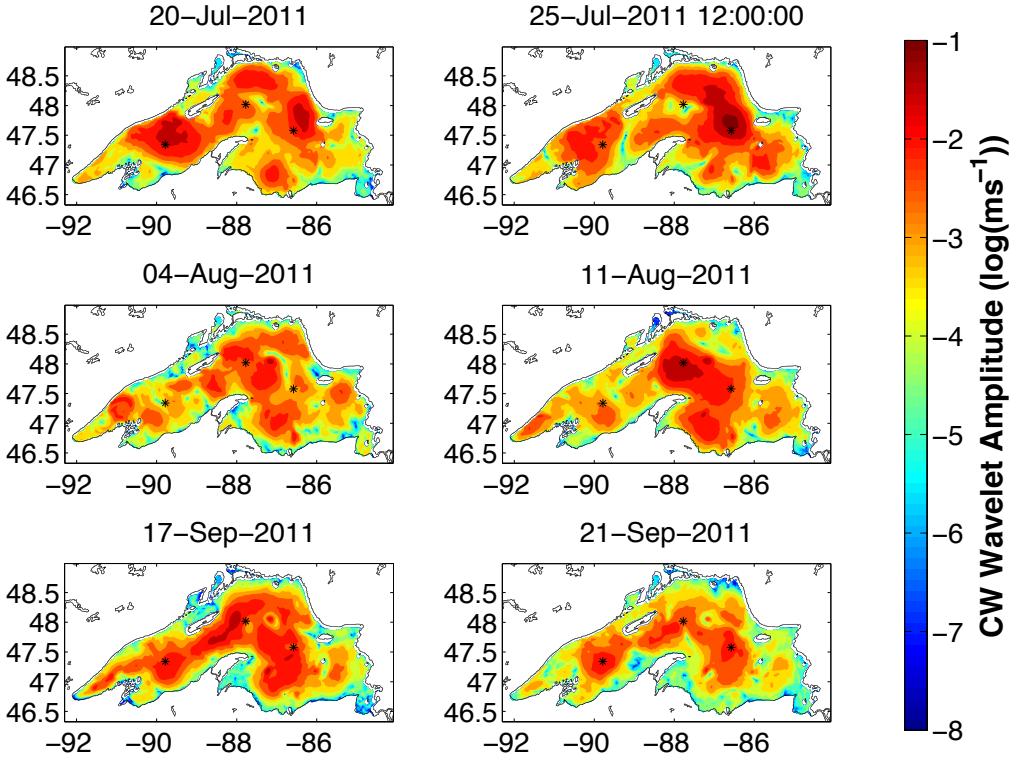

Figure 4.10: **Energy distribution: Realistic Bathymetry.** Surface kinetic energy distribution computed using the amplitude of clockwise rotary wavelet tuned to the inertial frequency. The cyan points are the core mooring sites. Each column is before and after a local inertial event

The surface kinetic energy was also calculated using the amplitude at the inertial frequency of the clockwise rotary spectrum. The spatial distribution of the inertial energy is given below.

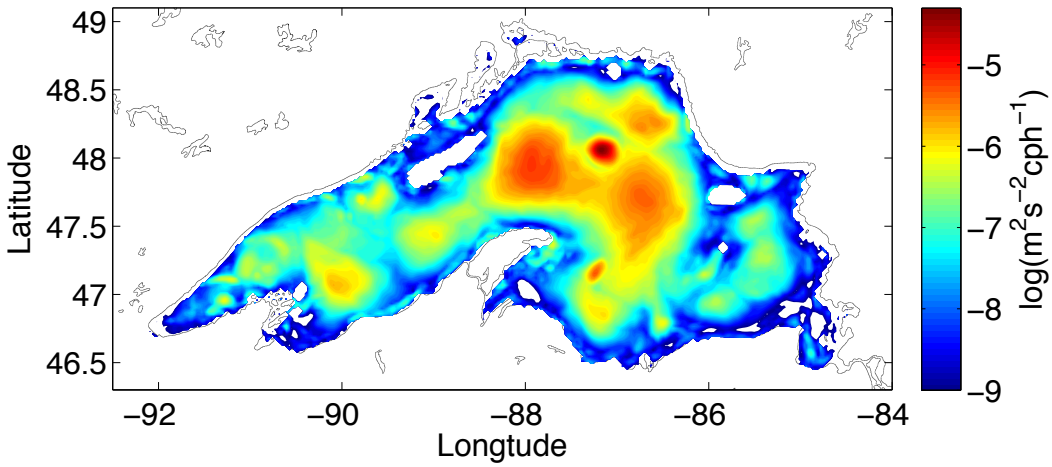

Figure 4.11: **Spatial Energy : Realistic Bathymetry.** Peak in the clockwise rotary spectrum at the Coriolis frequency.

Austin (2013) described a method to calculate the wavelength and wave direction of inertial waves based on the theory of a propagating plane wave in a two layer system. Below is a plot of the wavelength and wave direction based on the method described in Austin (2013).

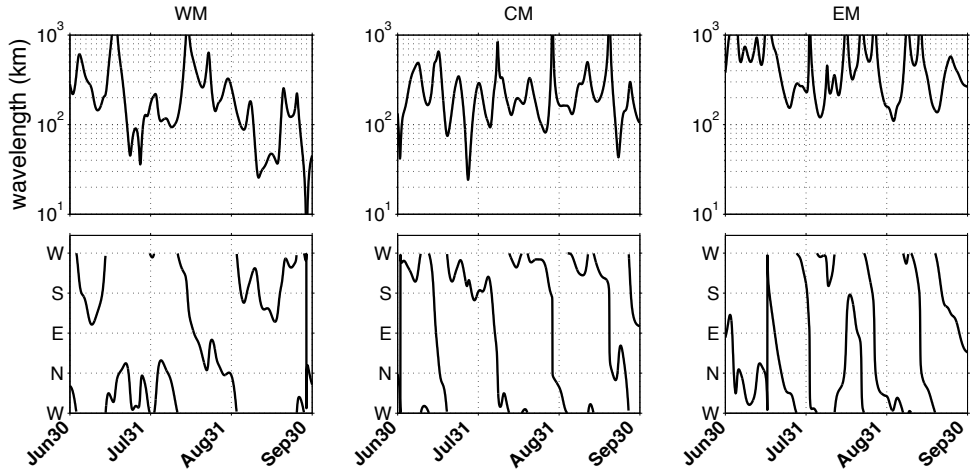

Figure 4.12: **Wave Climate : Realistic Bathymetry.** Estimated wavelength and wave direction at core mooring locations in the model. Each column is before and after a local inertial event

4.2 ADCP Observations

Near-inertial energy at the core mooring sites was quantified using ADCP observations. the complete record of upward looking ADCP observations at the core mooring sites is provided below.

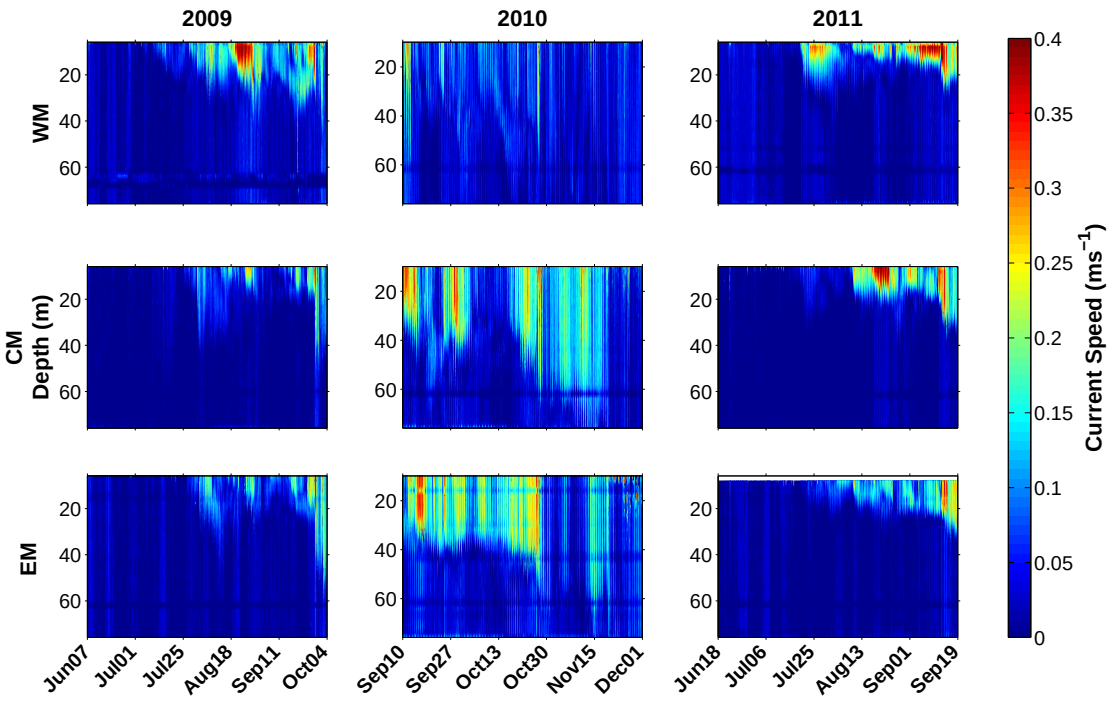

Figure 4.13: **Core Mooring ADCP Observations.** Three years worth of ADCP observations at the core mooring sites western mooring (WM, central mooring (CM), and eastern mooring (EM).

There are three periods where observations at all three mooring sites overlap.

- June, 7 2009 - October, 4 2009
- September, 10 2010 - December, 1 2010
- June, 18 2011 - September, 19 2011

These periods allow us to look at spatial variability among the sites for each period but does not permit a proper analysis of interannual variability. The surface currents were averaged over the top 15 m and the time series was then convoluted with wavelet tuned to the inertial frequency. A plot the overaged current and wavelet analysis is provided below.

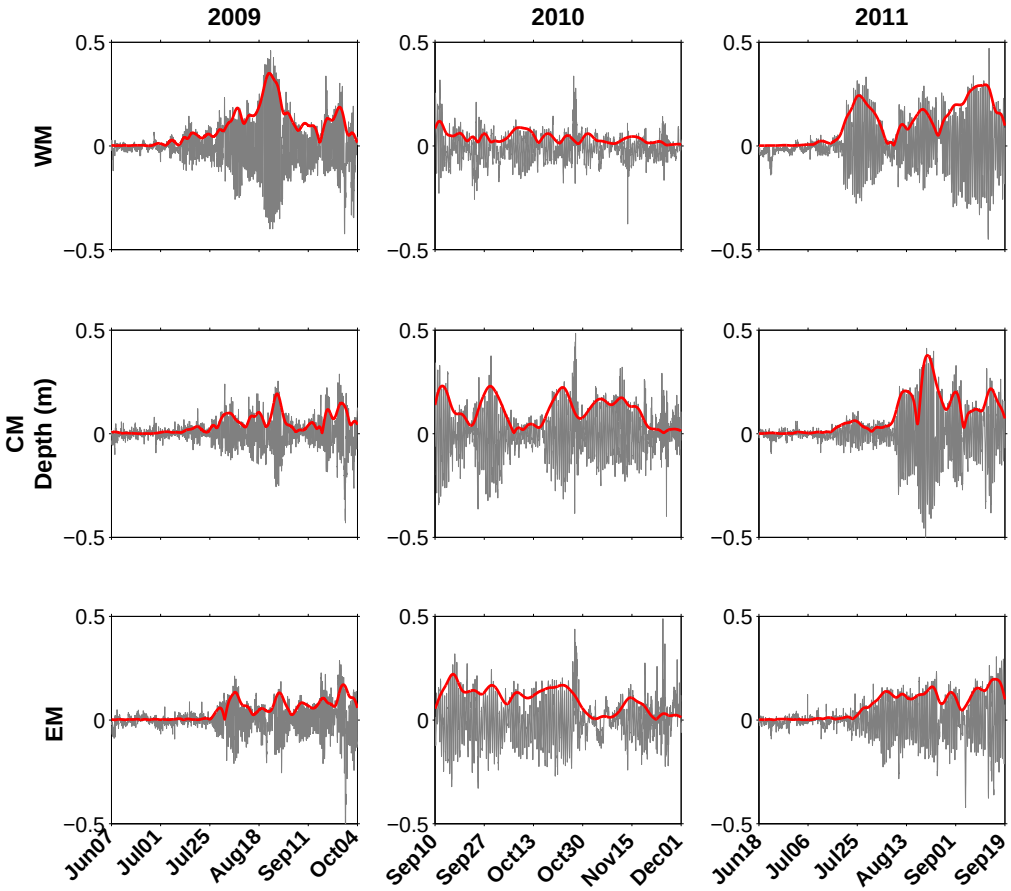

Figure 4.14: **Core Moorings Wavelet.** This plot shows the amplitude of the clockwise rotary wavelet tuned the inertial frequency. The amplitude can be thought of as the inertial velocity. This plot shows spatial variability between sites, but can not be used to show anything about inter annual variability.

The amplitude of the wavelet analysis is indicative of near-inertial currents and hence near-inertial kinetic energy. There appears to be a general coherence in near-inertial energy between sites during each period. When near near-inertial energy is high at one station it is relatively high at each other station. However, the partition of energy between sites is different for each period. During 2009 the inertial energy is greater at the western mooring while in 2010 there is less near-inertial energy at the western mooring compared to the other two. This suggests that although there appears to be coherence between the sites there is substantial spatial variability in the energy.

4.3 Comparison

Points in the Lake Superior NARR forcing model corresponding to the core mooring sites were compared with observations for the same period. Below is a plot comparing current speeds at each site.

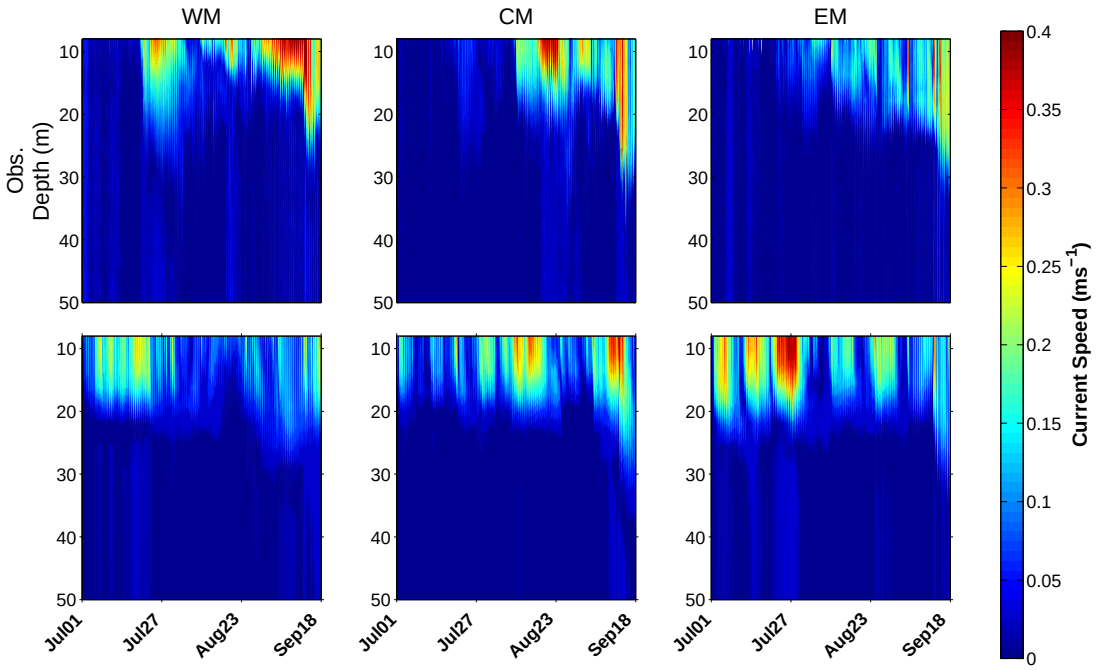

Figure 4.15: **Observational/ Model Comparison.** Comparison between currents speeds at core mooring locations and approximate location in the model.

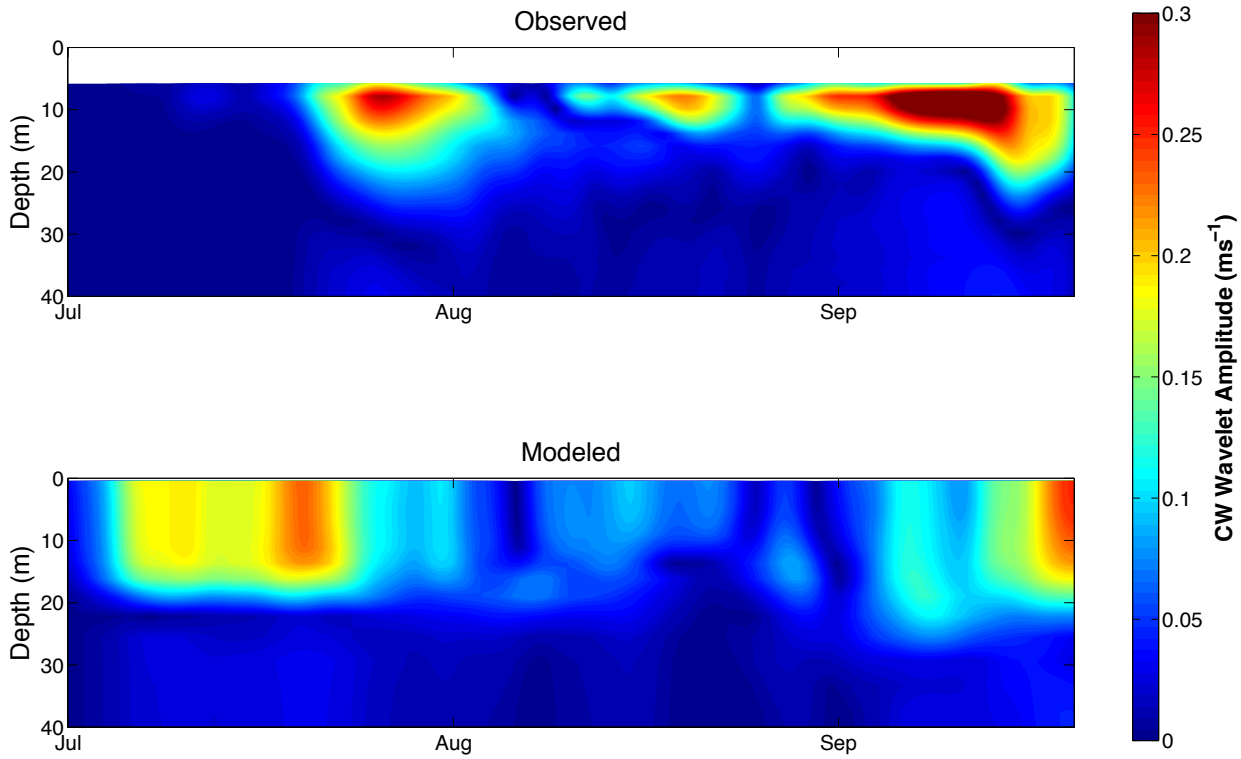

Figure 4.16: **Observational/ Modeled Wavelet Amplitude - WM.** The top plot shows the observed data between July 15, 2011 and September 15, 2011 at the western mooring while the bottom plot shows the modeled data during the same period.

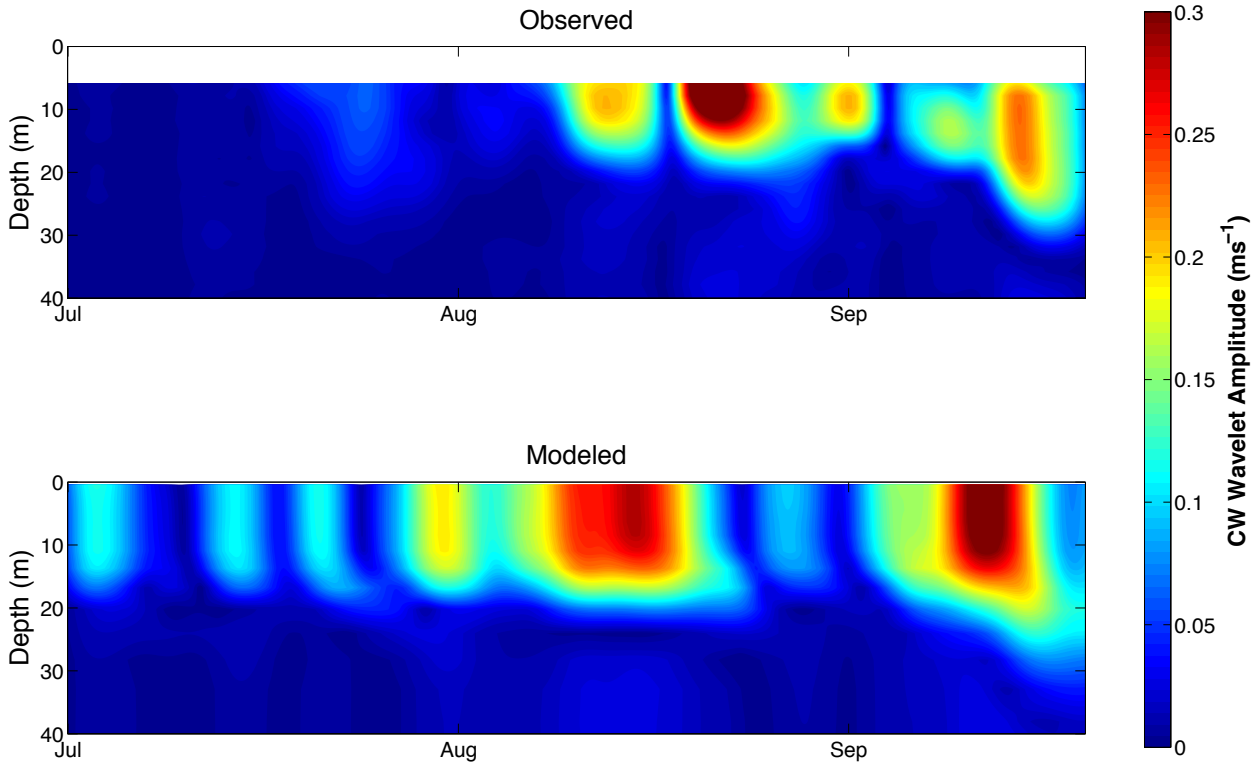

Figure 4.17: **Observational/ Modeled Wavelet Amplitude - CM.** The top plot shows the observed data between July 15, 2011 and September 15, 2011 at the central mooring while the bottom plot shows the modeled data during the same period.

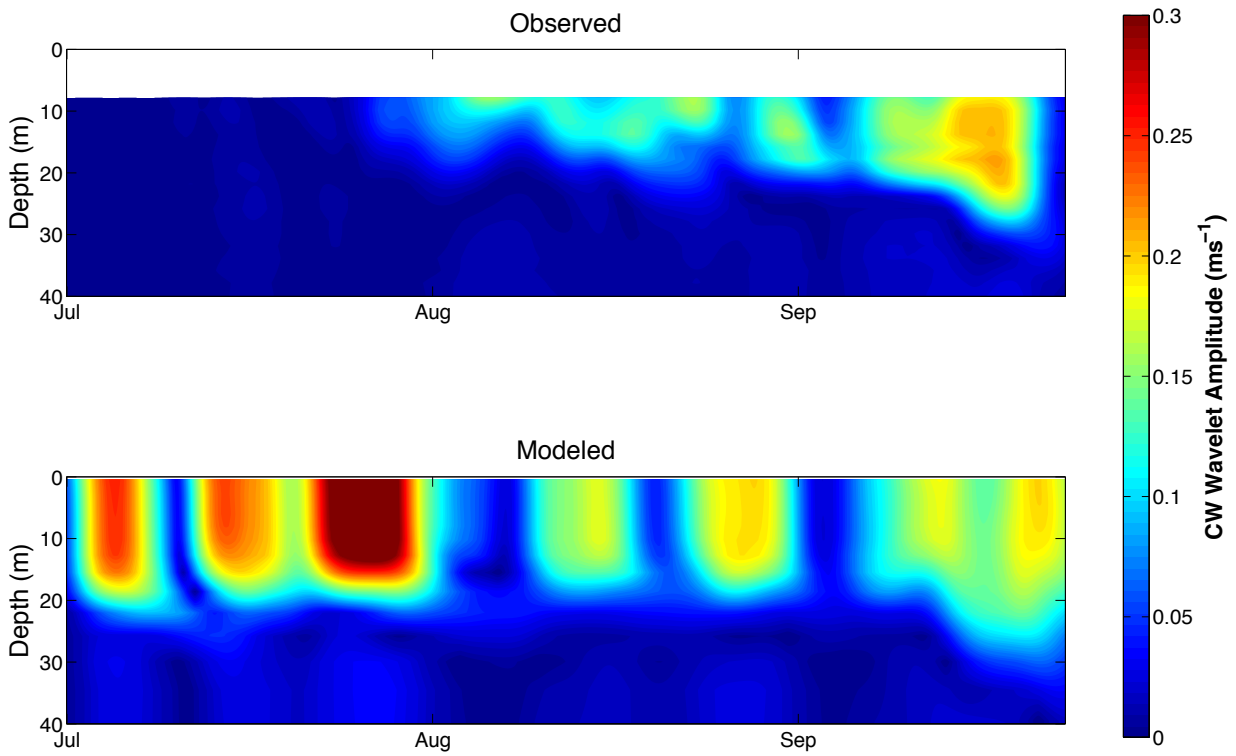

Figure 4.18: **Observational/ Modeled Wavelet Amplitude - EM.** The top plot shows the observed data between July 15, 2011 and September 15, 2011 at the eastern mooring while the bottom plot shows the modeled data during the same period.

Chapter 5

Discussion

5.1 Modeling

Accurately modeling near-inertial waves is difficult for a few reasons. The energy input to the model is highly dependent on the type of forcing used. Ideal forcing for half an inertial period is efficient at putting inertial energy into the system, however, ideal forcing puts little energy in above or below the Coriolis frequency. When spatially varying forcing is used the energy input below the Coriolis frequency agrees well with observational data. However, the energy deviates above the Coriolis frequency. The modeled inertial energy is also dependent on the initial phase of the currents before an inertial event.

In order to better understand the relationship between inertial energy and the duration of forcing a spectrum of model runs were done were done using a spatially uniform top-hat wind stress. The duration of the forcing varied from 1 hour up to 17 hours (approximately 1 inertial period). For each model run the magnitude of the wind stress was a constant $0.1Nm^{-2}$. When each model run was completed a rotary spectrum was applied to the first 256 hours of output after the forcing had stopped. The inertial energy was defined as the peak in the clockwise spectrum at the inertial frequency. The inertial energy as a function of the duration of forcing is shown in Figure 5.1 for three points in the flat-bottom square basin.

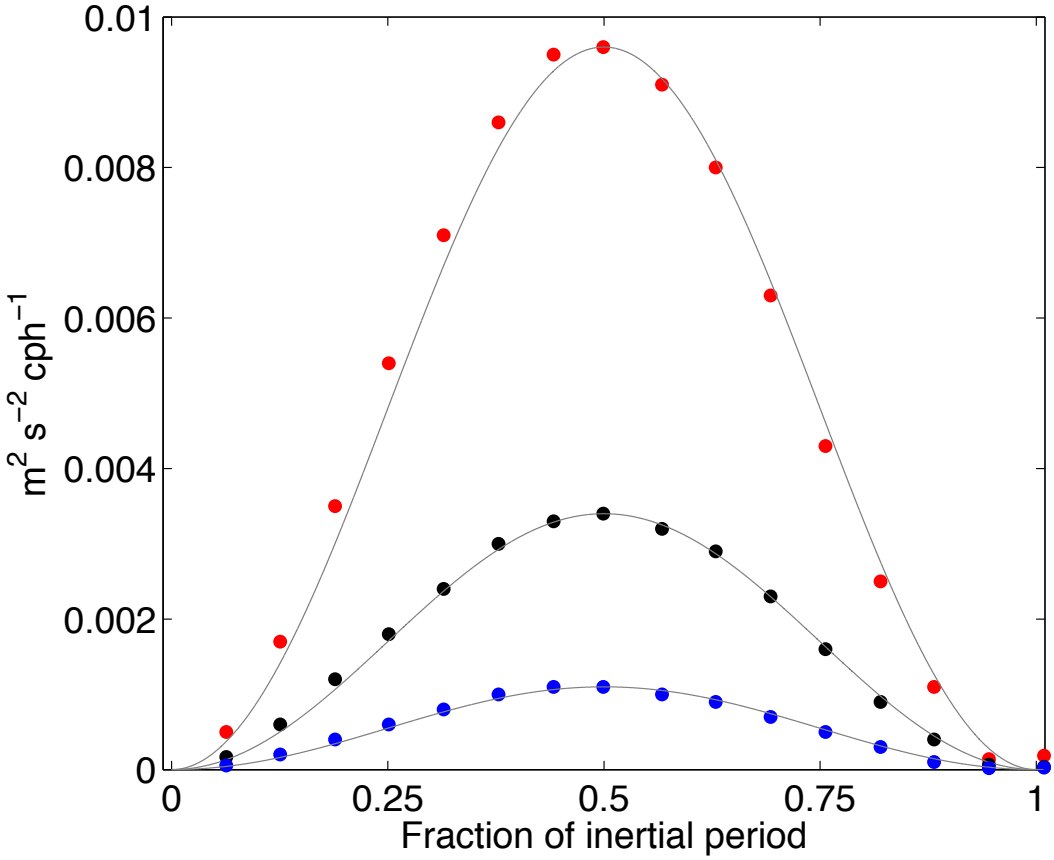

Figure 5.1: **Inertial Energy vs. Stress Duration.** This shows the peak in clockwise rotary spectral at the Coriolis frequency for various wind stresses.

This plot shows that when the most inertial energy is put into the system when the duration of forcing is half an inertial period and quelled when the duration of one inertial period. The distribution of energy follows a $\sin^2(\pi t)$ curve. This curve can be interpreted as the square of the inertial velocity divided by the Coriolis frequency. When the wind stress is applied to the surface the current vector will be pointing in the direction of the wind stress and will start to veer clockwise in the northern hemisphere (counterclockwise in the southern hemisphere). After half an inertial period the direction of the current will be 180° out of phase with the wind stress. In order for the wind stress to stop work needs to be done in the opposite direction of the stress. This work required to stop the wind stress increases the kinetic energy of the currents. When the stress is stopped

after one inertial period then work is being done against the current and kinetic energy is removed. This ideal is represented nicely with simple box model of the following set of equations :

$$\frac{du}{dt} = fv + \frac{\tau}{\rho} \tag{5.1}$$

$$\frac{dv}{dt} = fu \tag{5.2}$$

Where u and v are the zonal and meridional components of the current, τ is the wind stress, ρ is the density of water, and f is the Coriolis frequency. Figure 5.2 shows the results of the box model. When the wind stress stops after half an inertial period the amplitude of the currents are doubled.

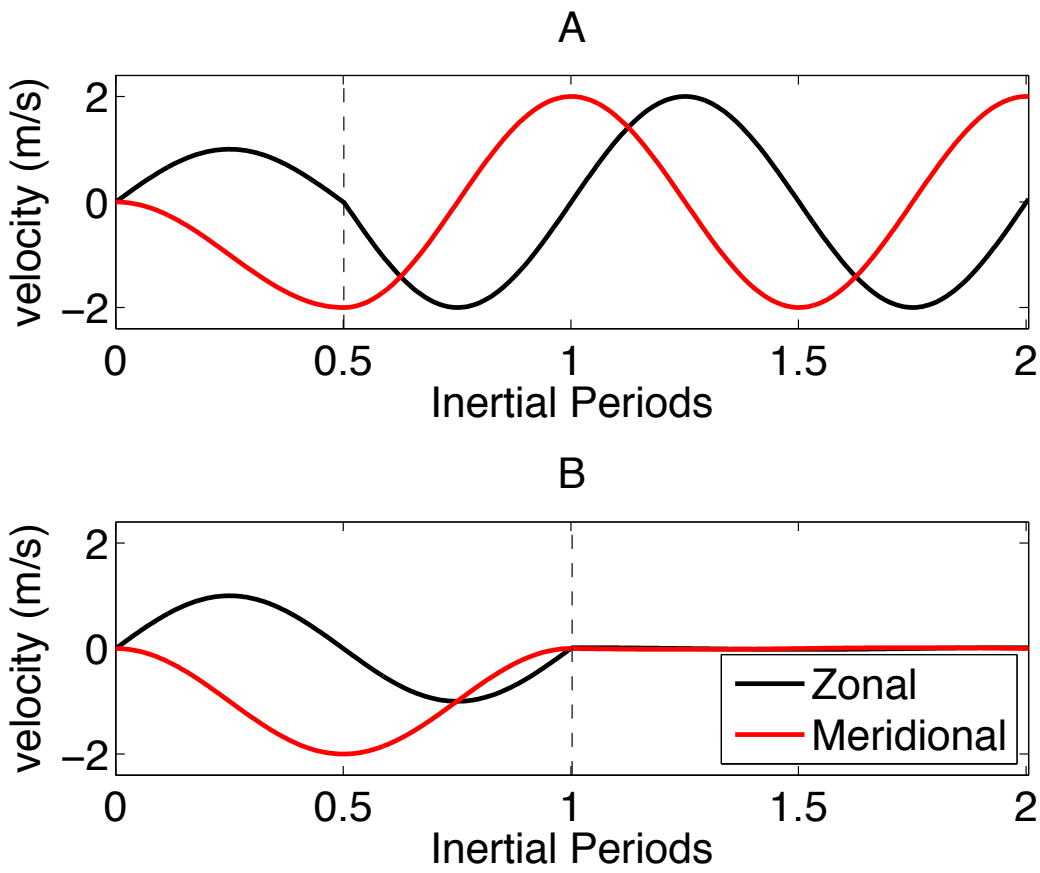

Figure 5.2: **Inertial Box Model.** Box model showing the zonal and meridional components when A) the wind stress is half an inertial period and B) when the wind stress is one inertial period.

The energy input at various frequencies is highly dependent on type of forcing used. Figure 5.3 shows a comparison between spectra of surface currents at the western mooring site using ideal forcing, spatially varying forcing, and observational data. The ideal forcing was a top-hat wind stress with a magnitude of $0.1Nm^{-2}$ and a duration of 8 hours (half the inertial period). The spatially varying forcing was derived from NARR wind velocities. Both forcing types agree well with observational data near the Coriolis frequency. At frequencies less than the Coriolis frequency the spatially varying forcing agrees quit well with observations but the ideal forcing is about four orders of magnitude lower. At frequencies greater than the Coriolis frequency the spatially

varying forcing deviates by about one order of magnitude and the ideal forcing deviates by about four orders of magnitude. The high energies outside the Coriolis frequency in the observations are presumably from wind forced frequencies. This explains the reduced energy in the ideal forcing and explains why the energy is amplified at the seiche frequencies. The seiche frequencies are standing waves in a basin that persist without wind.

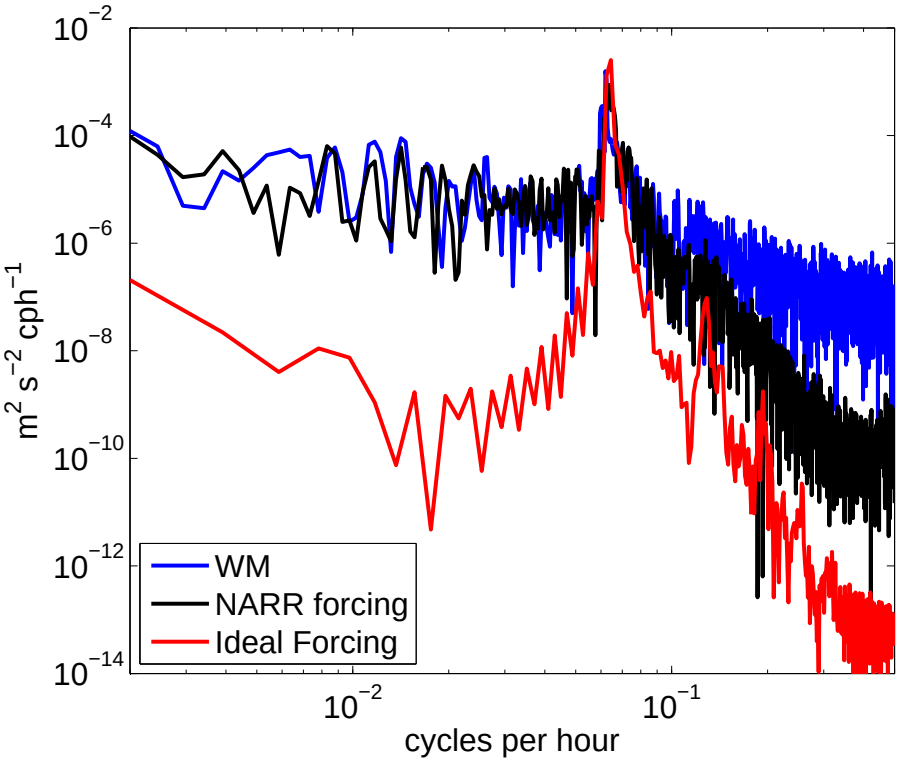

Figure 5.3: **Rotary Spectrum Comparison.** A comparison of spectrums from observation at the WM, forcing derived from NARR wind speeds, and ideal forcing.

5.2 Near-Inertial Energy

Near-inertial energy has large spatial and temporal variations in Lake Superior. Figure 4.14 shows ADCP observations from the core moorings for periods in 2009, 2010, and 2011. Large spatial variability in the near-inertial energy is observed during each period. An event July 24, 2011 put a large amount of inertial energy into the currents at the western mooring, but much weaker energy at the central and eastern mooring. However, there are events that appear weakly coherent at each location. An event on August 18, 2009 put a noticeable amount of energy in the system at all stations. However, the magnitude of the event varied at each location.

Understand how coherence works and do a coherence analysis between all possible combinations of sites. You have a coherence test in MATLAB but it appears to be dependent on the window width and window type. Do not know what to make of this.

5.2.1 Wind Field

Surface wind stress can put energy into NIWs as well as take energy away. One can not ascertain whether energy will be put into NIWs simply by looking at a time series of wind stress. In order for the wind stress to increase the kinetic energy of the current the wind needs to be doing positive work on the currents. In other words, there must be a component of the stress in the direction of the current. Because of this relationship between the current direction, wind stress, and energy input sometimes the modeled period does not coincide with observational data. For instance, an event July 24 2011 at the western mooring put a large amount of energy into the system, figure 4.14, while the modeled data showed energy decreased during this time. A comparison between the observed and modeled current at the western mooring is shown in figure **??**. The discrepancy arises since there is phase difference between the modeled current and the observed current. Inertial events prior to the onset of stratification caused the currents in the observations and model to become out of phase. This is clear by looking at the zonal component, figure 5.4, and meridional component, figure 5.5, during this event. On July 23rd, before the inertial event, the phase difference between the observations and model output are close to 180°, which means the effect of the wind event will have the opposite effect in the model as it does in observations. In order to accurately model

near-inertial waves the initial phase needs to be correct.

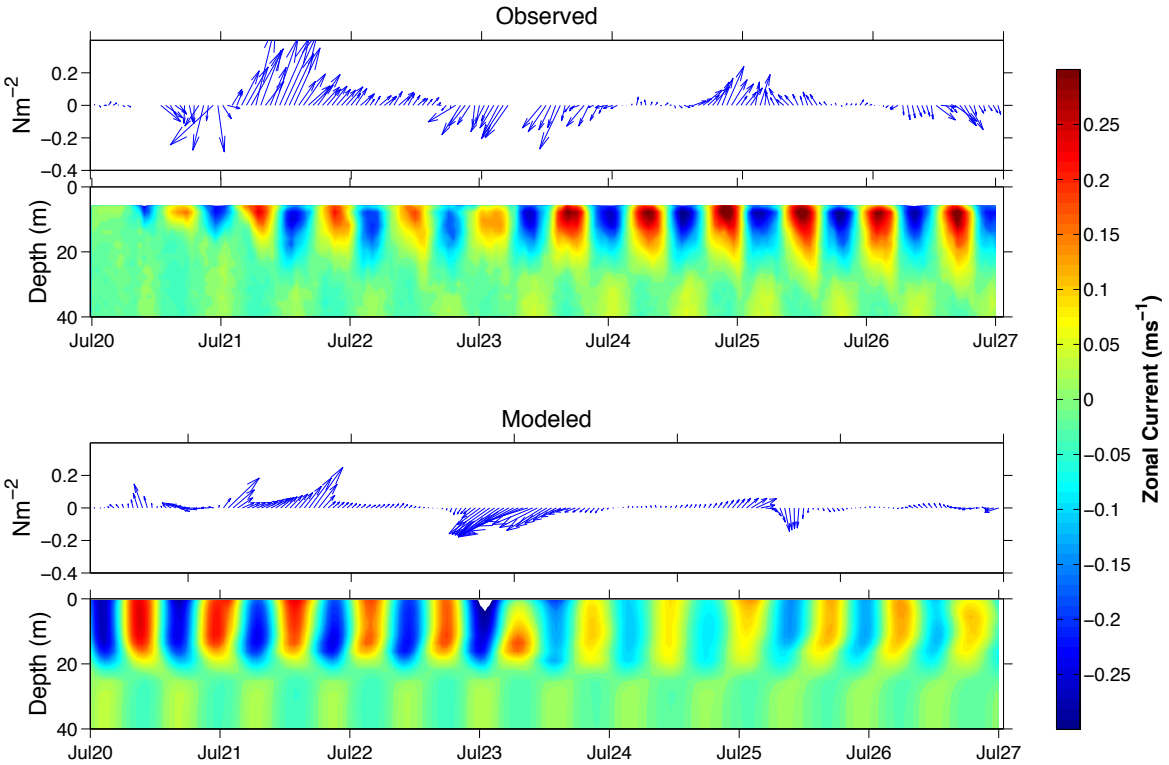

Figure 5.4: **Zonal Current Comparison.** Comparison between observed and modeled zonal currents during an observed inertial event.

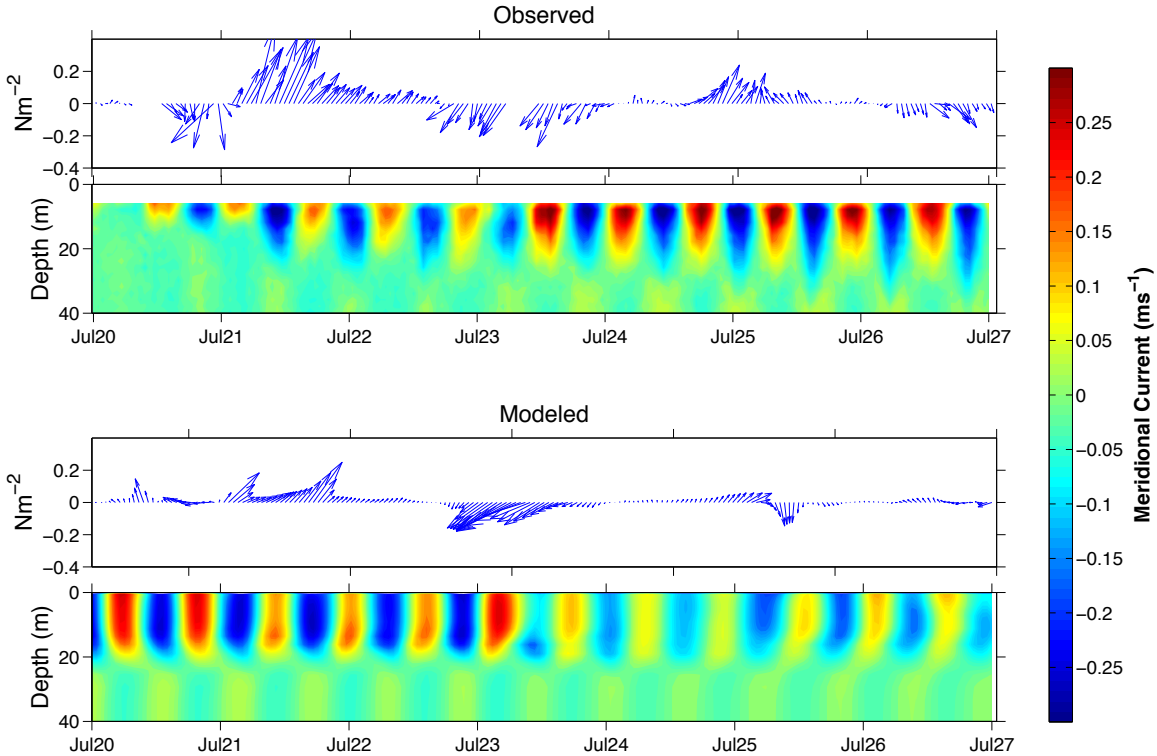

Figure 5.5: **Meridional Current Comparison.** Comparison between observed and modeled Meridional currents during an observed inertial event.

However, defining the time frame of the inertial event is difficult, even when you compare the wind stress vector to the surface current vector, figure 5.6. During this week the wind stress will predominately be in one direction for an extended period of time and if there is no phase lag between the wind stress and current vector then the wind stress will put energy after after half an inertial period and take some energy away during the next half inertial period and this process will repeat until the wind stress changes direction or stops.

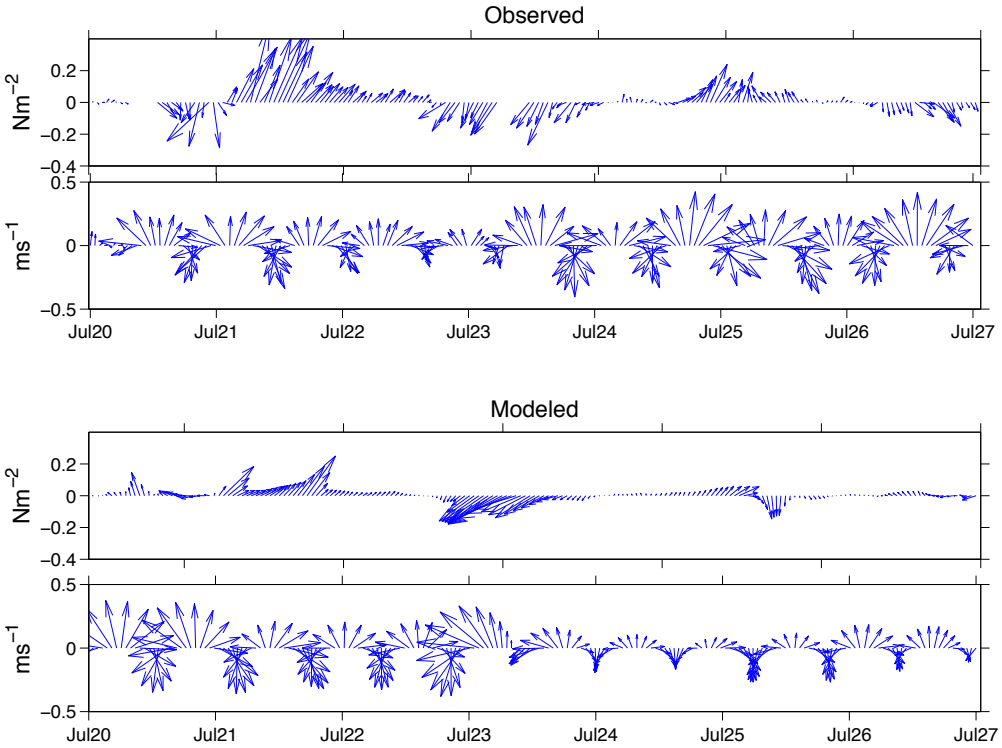

Figure 5.6: **Compare Wind Stress and Surface Current.** Comparison between observed and modeled wind stress and surface current vector. The top two panels show observations of surface stress and surface currents at the western mooring site. The bottom two panels show modeled output of surface stress and current vectors at the western mooring site.

Run a model where you remove 8 hours before the inertial event and see you get the opposite result.

5.3 Wave Climate

The wavelength and direction of propagation of NIWs were estimated following the same procedure as Austin (2013). Austin (2013) estimated the wavelength of NIWs to be between 30 km and 60 km during a large event at the end of July 2010. A large inertial event also occurred near the end of July 2011. The calculated wavelength during

this period was calculated to be around 60 km, figure 4.12. However, for most of the modeled period the wavelength of above 100 km. The modeled period also shows a slow counter-clockwise rotation with a period of about 30 days in the NIWs direction of propagation at all the mooring sites , figure 4.12. Austin (2013) calculated the same result and noted that this period is on the same order as the lowest order internal Kelvin wave.

5.4 Future Work

It is unclear whether large near-inertial events can be predicted with any real accuracy. A more realistic model would be needed in order to make predictions. The models presented in this thesis did not include radiative forcing so the thermocline can not evolve with time. The response of the bottom nephoid layer is another important area of research. NIWs have been correlated with the thickness in the bottom nephoid layer (Hawley 2004), however, this needs to be studied further. A physical model including sediment could be used to study the response of NIWs to various scenarios.

Chapter 6

Conclusions

6.1 Conclusions

- When using ideal, top-hat, wind stress the largest amount of inertial energy is put into the model when the duration of the forcing is half an inertial periods.
- Ideal forcing is good putting energy inertial energy in the system but puts little energy in at wind forced frequencies.
- In order to accurately model inertial events the initial phase needs to be properly assessed.
- Coherence between sites?

References

Sultan Ahmed, Cary D Troy, and Nathan Hawley. Spatial structure of internal poincaré waves in lake michigan. *Environmental Fluid Mechanics*, pages 1–21, 2013.

J.P Antenucci and J. Imberger. Energetics of long internal gravity waves in large lakes. *Limnol. Oceanogr.*, 46(7):1760:1773, 2001.

J.A Austin. Observations of near-inertial energy in lake superior. *Limnol. Oceanogr.*, 58(2):715–728, 2013. doi:10.4319/lo.2013.58.2.0715.

Richard P Barbiero and Marc L Tuchman. The deep chlorophyll maximum in lake superior. *Journal of Great Lakes Research*, 30:256–268, 2004.

J. R. Bennett. Characteristics of the thermal regime of lake superior. *J. Great Lakes. Res.*, 4(3-4):310:319, 1978.

JO Blanton. Some characteristics of nearshore currents along the north shore of lake ontario. *Journal of Physical Oceanography*, 4(3):415–424, 1974.

F. M. Boyce and F. Chiocchio. Inertial frequency current oscillations in the central basin of lake erie. *J. Great Lakes. Res.*, 13(4):542–558, 1987.

FM Boyce, MA Donelan, PF Hamblin, CR Murthy, and TJ Simons. Thermal structure and circulation in the great lakes. *Atmosphere-ocean*, 27(4):607–642, 1989.

FJ Bugnon and IA Whitehouse. Acoustic doppler current meter. *Oceanic Engineering, IEEE Journal of*, 16(4):420–426, 1991.

C-TA Chen and Frank J Millero. Precise thermodynamic properties for natural waters covering only the limnological range. *Limnology and Oceanography*, 31(3):657–662, 1986.

Jun Choi, Cary D Troy, Tsung-Chan Hsieh, Nathan Hawley, and Michael J McCormick. A year of internal poincaré waves in southern lake michigan. *Journal of Geophysical Research: Oceans (1978–2012)*, 117(C7), 2012.

John J Cullen. The deep chlorophyll maximum: comparing vertical profiles of chlorophyll a. *Canadian Journal of Fisheries and Aquatic Sciences*, 39(5):791–803, 1982.

VW Ekman. On dead-water. norw. n. polar exped. 1893-1896: Sci. results. *Christiania XV*, 1904.

Chris W Fairall, Edward F Bradley, David P Rogers, James Bearer Edson, and George S Young. Bulk parameterization of air-sea fluxes for tropical ocean-global atmosphere coupled-ocean atmosphere response experiment. *Journal of Geophysical Research*, 101(C2):3747–3764, 1996.

David M Glover, William J Jenkins, and Scott C Doney. *Modeling methods for marine science*. Cambridge University Press, 2011.

Andrés Gómez-Giraldo, Jörg Imberger, and Jason P Antenucci. Spatial structure of the dominant basin-scale internal waves in lake kinneret. *Limnology and oceanography*, 51(1):229, 2006.

Loren R Haury, Melbourne G Briscoe, and Marshall H Orr. Tidally generated internal wave packets in massachusetts bay. 1979.

Loren R Haury, Peter H Wiebe, Marshall H Orr, and Melbourne G Briscoe. Tidally generated high-frequency internal wave packets and their effects on plankton in massachusetts bay. *Journal of Marine Research*, 41(1):65–112, 1983.

N. Hawley. Response of the benthic nepheloid layer to near-inertial internal waves in southern lake michigan. *J. Geophys. Res.*, 109:C04007, 2004. doi:10.1029/2003JC002128.

PK Kundu and IM Cohen. Fluid mechanics. fourth edition, 2008.

George O Marmorino. Inertial current in lake ontario, winter 1972-73 (ifygl). *Journal of Physical Oceanography*, 8(6):1104–1120, 1978.

James McCulloch. The international field year for the great lakes. *Hydrological Sciences Journal*, 18(3):367–373, 1973.

Clifford Hiley Mortimer. Lake hydrodynamics. 1974.

RL Pickett and FP Richards. Lake ontario mean temperatures and currents in july 1972. *Journal of Physical Oceanography*, 5(4):775–781, 1975.

R. T. Pollard. On the generation by winds of inertial waves in the ocean. *Deep-Sea Res.*, 17:795–812, 1970.

R. T. Pollard and R. C. Millard Jr. Comparison between observed and simulated wind-generated inertial oscillations. *Deep-Sea Res.*, 17:813–821, 1970.

Hongbo Qi, Roland A De Szoeke, Clayton A Paulson, and Charles C Eriksen. The structure of near-inertial waves during ocean storms. *Journal of Physical Oceanography*, 25(11):2853–2871, 1995.

Francisco J Rueda, S Geoffrey Schladow, and Sveinn Ó Pálmarsson. Basin-scale internal wave dynamics during a winter cooling period in a large lake. *Journal of Geophysical Research: Oceans (1978–2012)*, 108(C3), 2003.

David J Schwab. Internal free oscillations in lake ontario. *Limnol. Oceanogr*, 22(4): 700–708, 1977.

David J Schwab and Diana L Sellers. *Computerized bathymetry and shorelines of the Great Lakes*. National Oceanographic and Atmospheric Administration, US Department of Commerce, Great Lakes Environmental Research Laboratory, 1996.

Peter W Sloss and James H Saylor. Large-scale current measurements in lake huron. *Journal of Geophysical Research*, 81(18):3069–3078, 1976.

RL Thomas and CI Dell. Sediments of lake superior. *Journal of Great Lakes Research*, 4(3):264–275, 1978.

Daniel James Titze. Observations of the winter thermal structure of lake superior. Master's thesis, University of Minnesota, 2013.